

## Research Article

# Chelated Nitrogen-Sulphur-Codoped TiO<sub>2</sub>: Synthesis, Characterization, Mechanistic, and UV/Visible Photocatalytic Studies

Hayat Khan,<sup>1,2</sup> Imran Khan Swati,<sup>2</sup> Mohammad Younas,<sup>2</sup> and Asmat Ullah<sup>2</sup>

<sup>1</sup>Department of Chemical Engineering, Polytechnique Montréal, Montréal, QC, Canada H3C 3A7

<sup>2</sup>Department of Chemical Engineering, University of Engineering and Technology Peshawar, University Campus, P.O. Box 814, Peshawar 25120, Pakistan

Correspondence should be addressed to Hayat Khan; [hayat.khan@polymtl.ca](mailto:hayat.khan@polymtl.ca)

Received 3 April 2017; Accepted 12 June 2017; Published 17 August 2017

Academic Editor: Juan M. Coronado

Copyright © 2017 Hayat Khan et al. This is an open access article distributed under the Creative Commons Attribution License, which permits unrestricted use, distribution, and reproduction in any medium, provided the original work is properly cited.

This study presents in detail the physicochemical, photoluminescent, and photocatalytic properties of carboxylic acid chelated nitrogen-sulphur-codoped TiO<sub>2</sub>. From the Fourier transform infrared spectroscopic study, it was revealed that the formate group formed bidentate bridging linkage while the acetate group coordinated in a bidentate chelating mode with a titanium precursor. In compliance with X-ray diffraction data, the anatase to rutile transformation temperature was extended due to carboxylic acid chelation and NS codoping. Raman analysis indicated four Raman peaks at 146, 392, 512, and 632 cm<sup>-1</sup> for the precalcined chelated TiO<sub>2</sub>; on incorporation with NS dopants, an increase in Raman intensity for these peaks was recorded, indicating the structure stability of the anatase phase. Furthermore, X-ray photoelectron spectroscopic study revealed the presence of anionic doping of nitrogen and cationic doping of sulphur in the lattice of TiO<sub>2</sub>. When evaluating the UV-visible photodegradation rate of 4-chlorophenol, the modified TiO<sub>2</sub> (NS<sub>0.06</sub>-TFA) showed the highest photocatalytic activity. In connection with the activity tests, several scavenger agents were employed to elucidate the significance of the different reactive oxidizing species during the photocatalytic process. Moreover, the transfer pathways of photogenerated carriers and the photocatalytic reaction mechanism of modified TiO<sub>2</sub> were also explained in detail.

## 1. Introduction

Titanium dioxide (TiO<sub>2</sub>) is an effective photocatalyst, which is widely studied for the degradation of organic pollutants in water after the discovery of the TiO<sub>2</sub>-photoassisted electrochemical splitting of water reported by Fujishima and Honda in 1972 [1]. TiO<sub>2</sub> exists in nature in three polymorphic forms (anatase, rutile, and brookite), which differ only in the arrangement of their TiO<sub>6</sub> octahedra; anatase (tetragonal) consists of octahedral shearing vertices; rutile (tetragonal) is connected by edges; and in brookite (orthorhombic), both edges and vertices are connected. Thermodynamically, rutile is the most stable phase while both anatase and brookite are metastable, transferring to rutile under heat

treatment, typically at temperature ranging between 600 and 700°C [2]. Among the TiO<sub>2</sub> crystalline forms, anatase and rutile are the most widely investigated polymorphs, with anatase generally found to be more photocatalytically active than brookite and rutile, but some reports illustrate the synergistic effect found in the composite mixture of anatase-brookite and anatase-rutile to be responsible for the enhanced photocatalytic activity [3, 4]. However, because of the large band gap, anatase (3.20 eV) begins to absorb UV light around 388.5 nm, and brookite (3.14 eV) absorbs at around 395 nm, whereas the absorption onset of rutile (3.02 eV) occurs around 411 nm [5]. Due to the UV absorption of TiO<sub>2</sub> polymorphs, their usage under visible light irradiation is greatly restricted. Therefore, research studies

begin to develop and synthesize  $\text{TiO}_2$  that can absorb and make use of both UV (290–400 nm) and visible (400–700 nm) light to enhance photocatalytic process efficiencies.

Many researchers have focused on modifying  $\text{TiO}_2$  with nonmetal nitrogen to be active in visible light irradiation; however, literature reports a different explanation for the decrease in N- $\text{TiO}_2$  band gap. For example, work by Asahi et al. [6] demonstrated that substitutional presence of nitrogen in the crystal lattice narrows the  $\text{TiO}_2$  band gap through N2p orbital mixing with O2p orbital. However, Ihara et al. [7] suggested that addition of nitrogen only increases the stabilization of oxygen vacancies and as a consequence helps to improve the visible light activity of N- $\text{TiO}_2$ . While, work by Irie et al. [8] showed that nitrogen atoms can be substituted for the lattice oxygen sites to form an isolated impurity energy level (N2p) above the valence band (O2p) of  $\text{TiO}_2$ , and under visible light, electrons are excited to the nitrogen impurity energy level. Many other research efforts have also been made with F, S, I, B, Br, C, Cl, and P to develop anionic-doped  $\text{TiO}_2$  with improved visible light activity [2, 9], and among these nonmetal dopants, sulphur doping in  $\text{TiO}_2$  has received much attention due to its anionic (sulfide,  $\text{S}^{2-}$ ) and cationic (hexavalent ( $\text{S}^{6+}$ ) and tetravalent ( $\text{S}^{4+}$ )) characteristics. However, literature showed controversial reports regarding the photocatalytic activity of cationic and anionic doping of sulphur in  $\text{TiO}_2$ . For example, Ohno et al. [10] reported that cationic S-doped  $\text{TiO}_2$  showed better visible light absorption and photocatalytic activity compared to anionic S-doped  $\text{TiO}_2$ ; in contrast, Sztatmary et al. [11] reported low UV photocatalytic activity of cationic S-doped  $\text{TiO}_2$  compared to Degussa P25. Chaudhuri and Paria [12] reported enhanced visible photocatalytic activity of anionic S-doped  $\text{TiO}_2$ , whereas the work of Rockafellow et al. [13] showed that sulphur atoms may act as deep hole trappers reducing the oxidizing power of the holes and hindering the generation of hydroxyl radicals. In spite of the extensive reports on cationic and anionic doping of  $\text{TiO}_2$ , the visible photocatalytic activity has remained quite low, because monodoping can generate recombination centers for the photoinduced electrons and holes inside the  $\text{TiO}_2$  [14]. To overcome the problem of electron-hole recombination, researchers tried codoping of  $\text{TiO}_2$  with both metals and nonmetals, and the results showed enhanced electron-hole separation and increased absorption of photons in the visible range leading to enhanced photocatalytic activity of codoped  $\text{TiO}_2$  against the degradation of aqueous organic compounds [15, 16].

$\text{TiO}_2$  synthesis by the sol gel method involves very rapid hydrolysis of titanium alkoxide with water due to their susceptibility to nucleophilic attack. The rate of hydrolysis and condensation reactions which govern  $\text{TiO}_2$  particle size, phase formation, and their transformation may be controlled by using chelating agents such as acetyl acetone, diols, acetic acid, urea, ammonium sulfate, and formic acid [17, 18]. The alkoxide stability improves control over the reaction conditions; recently, it was concluded that in the presence of a silver dopant, the chelation of formic acid with titanium was weakened which favors earlier phase transformation

[2]. In contrast, in the presence of vanadium ions, acetic acid favors bidentate chelating mode of linkage with titanium ions, and as a result, the transformation of anatase to rutile is suppressed [19]. In connection to such studies, it is hard to find a systematic study reporting the effect of nitrogen-sulphur codoping on carboxylic acid chelation, anatase to rutile transformation (ART), and UV-vis photocatalytic activity against the degradation of aqueous organic compounds; such work would be both scientifically and practically important. Therefore, the aim of the present work is to achieve the following objectives: (a) to develop a rapid, convenient, and simple preparation method for the synthesis of the photocatalyst; (b) to explain in a systematic way the binding mode behaviour of the two carboxylic acids such as formic and acetic acid with the alkoxide titanium precursor and the resulting effect on anatase to rutile transformation; and (c) to study the effect of an increase in molar concentration (mol%) of nitrogen-sulphur (NS) dopants on the physicochemical and UV-vis photocatalytic properties and on the hindrance of anatase to rutile transformation in carboxylic acid-modified  $\text{TiO}_2$ . Finally, to elucidate a systematic and comprehensive mechanism to discuss the transfer pathways of UV-vis-photoinduced charge carriers in regard to explaining the decrease in electron-hole recombination rate and enhanced activity of the codoped powders against the degradation of 4-chlorophenol (4-CP) as a model pollutant.

## 2. Experimental Materials and Methods

**2.1. Catalyst Preparation.** The nanoparticles of control and nitrogen-sulphur- (NS-) codoped  $\text{TiO}_2$  powders were prepared by sol-gel method. Titanium isopropoxide ( $\geq 97.0\%$  Aldrich), formic acid ( $\sim 98.0\%$ , Fluka), glacial acetic acid (ACS Fisher Scientific), and thiourea (99.0% extra pure Acros Organics) were used as received without any further purification process. Anhydrous ethyl alcohol was supplied by Commercial Alcohols (Boucherville, Quebec, Canada). Reverse osmosis water was used throughout this research.

In the typical experimental procedure for the synthesis of control  $\text{TiO}_2$ , a molar ratio of 1 : 3 : 2 : 18 among titanium isopropoxide (TTIP), formic acid ( $\text{CH}_2\text{O}_2$ ), anhydrous ethyl alcohol ( $\text{C}_2\text{H}_6\text{O}$ ), and water ( $\text{H}_2\text{O}$ ) was maintained. An appropriate volume of titanium isopropoxide (18 ml) was mixed with formic acid (7 ml) under strong magnetic stirring; for this solution, anhydrous ethyl alcohol (7 ml) was added dropwise under continuous stirring followed by the addition of water (18 ml). In the synthesis of nitrogen-sulphur-codoped  $\text{TiO}_2$ , measured amount of thiourea as dopant was added to water to form a uniform solution before added to the flask containing the mixed solution of formic acid, titanium isopropoxide, and anhydrous ethyl alcohol. Instantaneous hydrolysis reaction occurs in the reacting mixture due to the addition of water (with or without dopants) which resulted into a milky sol of hydrated titanium hydroxide. The sol solution was kept on constant magnetic stirring for 2 h and then aged for gelation for 5 h at room temperature followed by drying in oven at  $85^\circ\text{C}$  for 24 h. Finally, calcination was accomplished by firing the dried powders at  $700^\circ\text{C}$  for 1 h in air to form crystalline  $\text{TiO}_2$  nanoparticles.

The dopant, thiourea, was added in the concentrations of 0, 0.02, 0.04, 0.06, 0.08, and 0.1 mol%, and the final sample powders were referred as  $T_{FA}$  and  $(NS)_x-T_{FA}$ , where FA is formic acid, NS is nitrogen-sulphur dopants, and  $x$  is the dopant content (mol%). Similarly, control and nitrogen-sulphur-codoped catalyst powders were prepared following the same experimental procedure except using another acid catalyst; acetic acid and the final photocatalyst powders were labeled as  $T_{AA}$  and  $(NS)_x-T_{AA}$  where AA is acetic acid. In addition, to compare the chelating effect of the carboxylic acids, control  $TiO_2$  was also prepared by adding the required amount of water dropwise to the continuously magnetic stirred solution of titanium isopropoxide and ethyl alcohol. This photocatalyst powder was denoted by  $T_{control}$ .

**2.2. Characterization Details.** X-ray diffraction (XRD) patterns of control and doped  $TiO_2$  powders were recorded with Phillips PW 1710 diffractometer using monochromatic high intensity Cu  $K\alpha$  radiations ( $\lambda = 0.15418$  nm) at a scanning rate of  $0.03^\circ/\text{sec}$  and in the scanning range from  $10$  to  $80^\circ$ . The crystallite size ( $D$ ) was estimated using the Scherrer equation (1), and the rutile phase content was calculated using (2) [20]. The peak intensity of [101] of anatase and [110] of rutile reflections located at  $25.4^\circ$  and  $27.4^\circ$  on  $2\theta$  (degrees)  $x$ -axis was used.

$$D = \frac{0.9\lambda}{\beta \cos\theta}, \quad (1)$$

where  $k$  is a constant equal to 0.9,  $\lambda$  equal to  $1.5418 \text{ \AA}$  is the X-ray wave length of Cu,  $\beta$  is full width at half maximum (FWHM) of the peak, and  $\theta$  is the Bragg's angle in radians.

$$\text{Rutile phase \%} = \frac{A_R}{0.884A_A + A_R}, \quad (2)$$

where  $A_A$  and  $A_R$  represent the integrated intensities of anatase and rutile peaks.

High-resolution transmission electron microscope (HRTEM) images of the prepared samples were observed with Phillips CM200 TEM operated at 200 kV. Infrared spectra (IR) was recorded on a Bruker Tensor 27 FTIR with OPUS data collection program (V 1.1); the energy range of  $5000\text{--}400 \text{ cm}^{-1}$  was used to evaluate the carboxylate-binding mode and the presence of different bonding vibrational frequencies; the precalcined and calcined catalyst powder was mixed with the reference potassium bromide (KBr). The thermogravimetric analysis was carried out with an apparatus (TGA-7) from Perkin Elmer (Norwalk, CT, USA) in the temperature range from  $20^\circ\text{C}$  to  $800^\circ\text{C}$  at a heating rate of  $10^\circ\text{C}\cdot\text{min}^{-1}$ ; the experiments were carried out on  $15\text{--}20$  mg specimen under nitrogen atmosphere ( $40 \text{ ml/min}$ ). Raman spectra were acquired at room temperature using a SENTERRA confocal Raman microscope (Bruker, US) equipped with a  $532 \text{ nm}$  laser. Room temperature photoluminescence spectrum (PL) was recorded with FluroMax-2 spectrofluorometer at an excitation wavelength of  $310$  and  $410 \text{ nm}$ . Carry 5000 NIR UV-vis spectrophotometer (Varian Inc., US) with attached Praying Mantis™ diffuse

reflection (DRIFTS) accessory was used to record absorption and diffuse reflectance spectra (DRS) in the range  $190\text{--}800 \text{ nm}$ ; catalyst powder was mixed in KBr and pressed into a tablet; a KBr tablet made under the same conditions was used as a reference. The oxidation state and elemental compositions of the doping metals were analyzed using X-ray photoelectron spectroscopy (XPS, Thermo Scientific K-alpha, USA) using an X-ray source of  $AlK\alpha$  ( $1486.6 \text{ eV}$ ). A survey spectrum was first recorded to identify all the elements present in the powder using a spot size of  $300 \mu\text{m}$  and step size of  $1.00 \text{ eV}$ , followed by recording high-resolution spectra of the identified elements using a step size of  $0.1 \text{ eV}$ . Data spectrum processing was performed using the Avantage (Thermo Scientific) software.

The room temperature photocatalytic activities of the prepared catalyst powder were investigated for the degradation of 4-chlorophenol (4-CP) as a model pollutant. The cylindrical reactor contained  $21$  aqueous solution of  $0.007 \text{ g}\cdot\text{l}^{-1}$  of 4-CP and  $0.1 \text{ g}\cdot\text{l}^{-1}$  of the prepared powder. A single UV light source (max. output at  $254 \text{ nm}$ , TUV 11 W 4P-SE, UV-Technik Speziallampen GmbH, Germany) protected in a quartz sleeve was placed vertically at the center point inside the reactor. The reactor solution under constant magnetic stirring was bubbled continuously with purified external air throughout the experiment. UV illumination was supplied for one-hour experimental duration. A sample of  $5 \text{ ml}$  was withdrawn at regular interval; before analysis, the sample suspension was filtered to remove the photocatalyst particles. The photocatalytic degradation of 4-CP was determined by performing the HPLC analysis procedure as stated elsewhere [21].

In the visible photocatalytic experiments, the reactor suspension was  $11$ , and the concentration of 4-CP and the photocatalyst powder was kept the same as used in the UV experiments. The reactor solution was irradiated with visible light for  $12 \text{ min}$  experimental duration using a single  $180 \text{ W}$  Hg-medium pressure lamp ( $\lambda = 420\text{--}660 \text{ nm}$ , intensity  $100 \text{ mW/cm}^2$ ) supplied by Heraeus Nobel Light, Germany; protected in a quartz sleeve and mounted vertically at the center point inside the reactor, a UV blocking film (UVPS, USA) was used to eliminate any UV radiations in the emitted light. Moreover, the temperature of reactor suspension was maintained in the range of  $25\text{--}30^\circ\text{C}$  with cold circulating water. The pH of the reactor suspension was measured with Fisher AccumetTMAB15 pH meter equipped with a glass pH electrode, and a constant pH of  $5.5\text{--}5.7$  was measured throughout the photocatalytic activity experiments.

### 3. Results and Discussion

**3.1. X-Ray Diffraction (XRD).** Figure 1(a) shows the XRD patterns of control  $TiO_2$  prepared in the absence and in the presence of carboxylic acids (acetic acid and formic acid) and calcined at  $700^\circ\text{C}$ . Rutile (99.0 wt.%) was the main phase in  $T_{control}$  powder while  $T_{FA}$  powder contained anatase (11.0 wt.%) and rutile (89.0 wt.%) phases, and  $T_{AA}$  powder was composed solely of the anatase phase. Figure 1(b) illustrates the XRD patterns of codoped  $(NS)_x-TiO_2$  powders employing carboxylic acids in the synthesis process, and

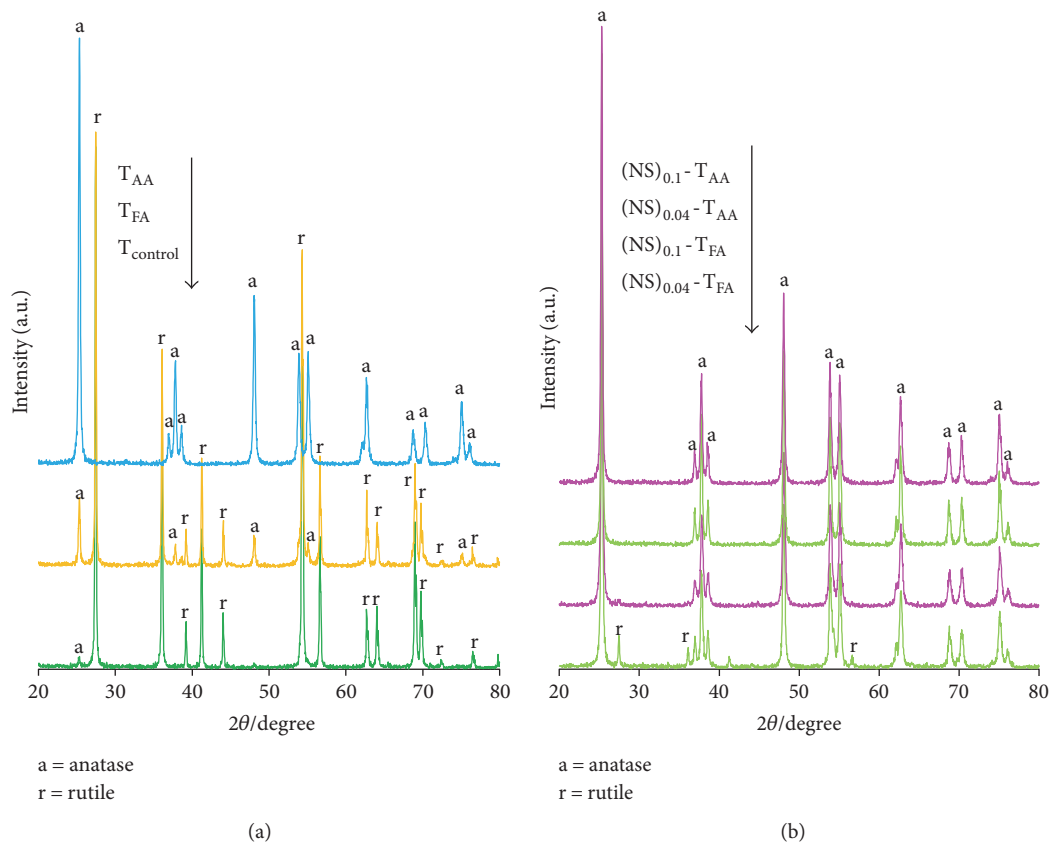


FIGURE 1: X-ray diffraction patterns of (a)  $T_{\text{control}}$ ,  $T_{\text{FA}}$ , and  $T_{\text{AA}}$  and (b)  $(\text{NS})_{0.04}\text{-}T_{\text{FA}}$ ,  $(\text{NS})_{0.1}\text{-}T_{\text{FA}}$ ,  $(\text{NS})_{0.04}\text{-}T_{\text{AA}}$ , and  $(\text{NS})_{0.1}\text{-}T_{\text{AA}}$  powders calcined at  $700^{\circ}\text{C}$ .

TABLE 1: Crystallite size, phase fractional compositions (values shown in parentheses), anatase phase lattice parameters, and band gap values of control and carboxylic acid modified NS-codoped  $(\text{NS})_x\text{-}T_{\text{FA}}$  and  $(\text{NS})_x\text{-}T_{\text{AA}}$  (where  $x = 0, 0.02, 0.04, 0.06, 0.08,$  and  $0.1$ )  $\text{TiO}_2$  powders calcined at  $700^{\circ}\text{C}$ .

Photocatalyst powder	Anatase crystallite size (nm)	Rutile crystallite size (nm)	Anatase lattice parameters ( $\text{\AA}$ )		Band gap (eV)
			$a = b$	$c$	
$T_{\text{control}}$	35.0 (0.01)	55.7 (0.99)	3.79	9.48	3.02
$T_{\text{FA}}$	31.0 (0.11)	55.4 (0.89)	3.79	9.53	3.04
$\text{NS}_{0.02}\text{-}T_{\text{FA}}$	39.4 (0.47)	55.4 (0.51)	3.79	9.52	3.06
$\text{NS}_{0.04}\text{-}T_{\text{FA}}$	34.2 (0.91)	55.4 (0.09)	3.78	9.59	2.92
$\text{NS}_{0.06}\text{-}T_{\text{FA}}$	31.4 (0.93)	46.2 (0.07)	3.79	9.61	2.75
$\text{NS}_{0.08}\text{-}T_{\text{FA}}$	28.6 (0.96)	46.2 (0.04)	3.78	9.67	2.60
$\text{NS}_{0.1}\text{-}T_{\text{FA}}$	24.0 (1.00)		3.79	9.69	2.52
$T_{\text{AA}}$	40.0 (1.00)		3.78	9.49	3.15
$\text{NS}_{0.02}\text{-}T_{\text{AA}}$	45.4 (1.00)		3.78	9.48	3.10
$\text{NS}_{0.04}\text{-}T_{\text{AA}}$	45.6 (1.00)		3.79	9.51	3.00
$\text{NS}_{0.06}\text{-}T_{\text{AA}}$	45.2 (1.00)		3.78	9.49	2.89
$\text{NS}_{0.08}\text{-}T_{\text{AA}}$	45.4 (1.00)		3.78	9.54	2.76
$\text{NS}_{0.1}\text{-}T_{\text{AA}}$	44.7 (1.00)		3.79	9.56	2.70

$(\text{NS})_{0.04}\text{-}T_{\text{FA}}$  powder is comprised of mainly anatase (92.0 wt.%) with a minor rutile (8.0 wt.%) phase, while  $(\text{NS})_{0.1}\text{-}T_{\text{FA}}$  consists only of the anatase phase; similarly, the

powders  $(\text{NS})_{0.04}\text{-}T_{\text{AA}}$  and  $(\text{NS})_{0.1}\text{-}T_{\text{AA}}$  were composed of pure anatase. The weight fraction of anatase and rutile phases of the prepared samples given in Table 1 illustrates that the

inclusion of and an increase in NS in  $\text{TiO}_2$  crystal lattice decrease the percentage of rutile phase in the final powders, indicating that the anatase phase has better thermal stability after NS codoping. Our results contradict the reported results of Nolan et al. [22] stating that addition of nitrogen increases the rutile percentage.

Further studying the effect of doping, crystal lattice distortion was observed as indicated from the change in anatase lattice parameter “c” (Table 1) meaning that variation in interatomic distances has occurred [23]. Thus, on doping, the Ti-O bonds will break and may reduce in numbers, implying that the number of octahedron molecules for rutile structure formation decreases, and as a result, rutile phase formation gets restrained. Moreover, anatase to rutile transformation (ART) is strongly particle size dependent [20]. Table 1 illustrates the crystallite sizes of the prepared powders; compared to control  $\text{TiO}_2$  ( $T_{\text{control}}$ ,  $T_{\text{FA}}$ , and  $T_{\text{AA}}$ ), an increased inclusion of the dopants in  $\text{TiO}_2$  lattice causes a decrease in the crystallite size of the samples ( $(\text{NS})_x\text{-}T_{\text{FA}}$ ) employing formic acid. However, in acetic acid-modified samples ( $(\text{NS})_x\text{-}T_{\text{AA}}$ ), no observable change in the crystallite size was noticed. This result indicates that NS codoping restrains the crystallite growth of codoped  $\text{TiO}_2$ , so does the phase transformation. Defect concentration and grain boundary concentration can also govern phase transformation [24]; the influence of such effects increases with an increase in crystallite size via decrease in surface area. In addition to the restrained growth of the codoped  $\text{TiO}_2$  crystallites, the similarity in the ionic radii of nitrogen ( $\text{N}^{3-}$ , 0.15 nm) to oxygen ( $\text{O}^{2-}$ , 0.14 nm) and that of sulphur ( $\text{S}^{6+}$ , 0.03 nm and  $\text{S}^{4+}$ , 0.04 nm) to titanium ( $\text{Ti}^{4+}$ , 0.07 nm) further illustrates that nitrogen and sulphur dopants can substitute into the  $\text{TiO}_2$  lattice, which minimizes the chance of NS migration to the anatase grain surface on calcination. As a consequence, surface defects in the anatase grain will decrease, which favors the decrease in anatase to rutile phase transformation.

Figure 2 shows the representative HRTEM images of  $T_{\text{control}}$  (a),  $(\text{NS})_{0.06}\text{-}T_{\text{FA}}$  (b), and  $(\text{NS})_{0.06}\text{-}T_{\text{AA}}$  (c) powders. The particle sizes measured with TEM for all the samples were consistent with the XRD results. The high-resolution images of all the powders clearly show the crystalline nature of the material; moreover, the lattice fringe spacing of 0.35 nm corresponds to a [110] crystallographic plane of rutile in  $T_{\text{control}}$  powder (Figure 2(d)), while 0.36 and 0.34 nm corresponds to the [101] plane of anatase in  $(\text{NS})_{0.06}\text{-}T_{\text{FA}}$  and  $(\text{NS})_{0.06}\text{-}T_{\text{AA}}$  (Figures 2(e) and 2(f)) powders, respectively.

**3.2. Fourier Transform Infrared Spectroscopy (FTIR).** Fourier transform infrared spectroscopy analysis was carried out to study the interaction of formic and acetic acid with a titanium precursor (TTIP) in the absence and presence of NS dopants. Figures 3(a) and 3(b) show the infrared spectra of the precalcined powders:  $T_{\text{control}}$ ,  $T_{\text{FA}}$ ,  $(\text{NS})_{0.06}\text{-}T_{\text{FA}}$ ,  $(\text{NS})_{0.1}\text{-}T_{\text{FA}}$ ,  $T_{\text{AA}}$ ,  $(\text{NS})_{0.06}\text{-}T_{\text{AA}}$ , and  $(\text{NS})_{0.1}\text{-}T_{\text{AA}}$ . The broad absorption band ( $2800\text{--}3600\text{ cm}^{-1}$ ) centered at  $3178\text{ cm}^{-1}$  indicates hydroxyl group stretching vibrations. In the region below  $1000\text{ cm}^{-1}$ , several peaks were ascribed to absorption

bands of Ti-O-Ti, Ti-O, and O-Ti-O flexion vibrations. The IR spectrum of  $T_{\text{control}}$  showed a sharp peak at  $1635\text{ cm}^{-1}$  attributed to H-O-H bending vibration mode of physisorbed water. This peak is shifted to lower frequencies in the samples employing the carboxylic acids. The powders ( $T_{\text{FA}}$ ,  $(\text{NS})_{0.06}\text{-}T_{\text{FA}}$ , and  $(\text{NS})_{0.1}\text{-}T_{\text{FA}}$ ) showed sharp peaks at  $1573$  and  $1357\text{ cm}^{-1}$  representing  $\nu(\text{COO}^-)_{\text{asym}}$  and  $\nu(\text{COO}^-)_{\text{sym}}$  carboxylate stretches, respectively. Zelenak et al. [25] determined the mode of binding of the carboxylate group to the metal atom by calculating the difference ( $\Delta$ ) in the values of carboxylate stretches,  $\Delta = \nu(\text{COO}^-)_{\text{asym}} - \nu(\text{COO}^-)_{\text{sym}}$ . From the spectra (Figure 3(a)),  $\Delta = 216\text{ cm}^{-1}$  indicating that the formate group is bound with the titanium precursor by a bidentate bridging mode; the proposed scheme I is shown in Figure 4. The IR spectra of the samples ( $T_{\text{AA}}$ ,  $(\text{NS})_{0.06}\text{-}T_{\text{AA}}$ , and  $(\text{NS})_{0.1}\text{-}T_{\text{AA}}$ ) employing acetic acid in the synthesis procedure are shown in Figure 3(b); the  $T_{\text{AA}}$  sample showed a peak at  $1712\text{ cm}^{-1}$  assigned to the stretching vibration of  $\nu(\text{C-O})$  of the COOH group, and the peak at  $1265\text{ cm}^{-1}$  is attributed to the symmetric bending vibration of the  $\text{CH}_2$  group or to the bending vibration of the  $\text{CH}_3$  group. Both of these peaks were weakened in the NS-codoped samples illustrating the inclusion of the dopant into the crystal lattice, while the weak shoulder at  $1020\text{ cm}^{-1}$  may indicate the presence of carbonyl moieties coming from isopropoxide residues. The carboxylate peaks appear at  $1536$  and  $1436\text{ cm}^{-1}$  which represent asymmetric carboxylate stretching ( $\nu(\text{COO}^-)_{\text{asym}}$ ) and symmetric carboxylate stretching ( $\nu(\text{COO}^-)_{\text{sym}}$ ), respectively [26, 27]. The difference between these two carboxylate stretches gives the value of  $\Delta = 100\text{ cm}^{-1}$ , illustrating that the acetate group is bound to titanium atoms through bidentate chelating modes, and the proposed scheme II is shown in Figure 4. Moreover, the weak shoulder at  $1620\text{ cm}^{-1}$  in the samples ( $(\text{NS})_{0.06}\text{-}T_{\text{AA}}$  and  $(\text{NS})_{0.1}\text{-}T_{\text{AA}}$ ) is attributed to the O-H bending vibration mode showing that NS-codoped powders are more susceptible to OH groups.

The above analysis shows that under the same synthesis conditions and using the same molar (mol%) amount of carboxylic acid, formic acid, and acetic acid formed different types of binding linkages with the titanium precursor, and this is the reason why the samples behave in different ways to the phase transformation. It is obvious that titanium alkoxide modification with chelating agents (formic and acetic acid) could promote anatase phase at increased temperature. In compliance with the XRD data (Figure 1(a)),  $T_{\text{AA}}$  powder is pure anatase, while  $T_{\text{FA}}$  powder is composed of both anatase and rutile phases, demonstrating that the chelating structure of the acetates promotes the formation of polymeric chains with extensive cross-linking in comparison to the bridging structure of the formate group. These chains remain stable throughout much of the condensation process; as a consequence, anatase-rutile transformation temperature is extended. In contrast, in the absence of chelating acids, weak gel networks are formed in the powder  $T_{\text{control}}$ ; only the addition of water causes increased hydrolysis which results in the formation of larger particles that thermodynamically favor phase transformation to rutile [2]. The observed results were further supported by the thermal analysis of the precalcined powders as explained

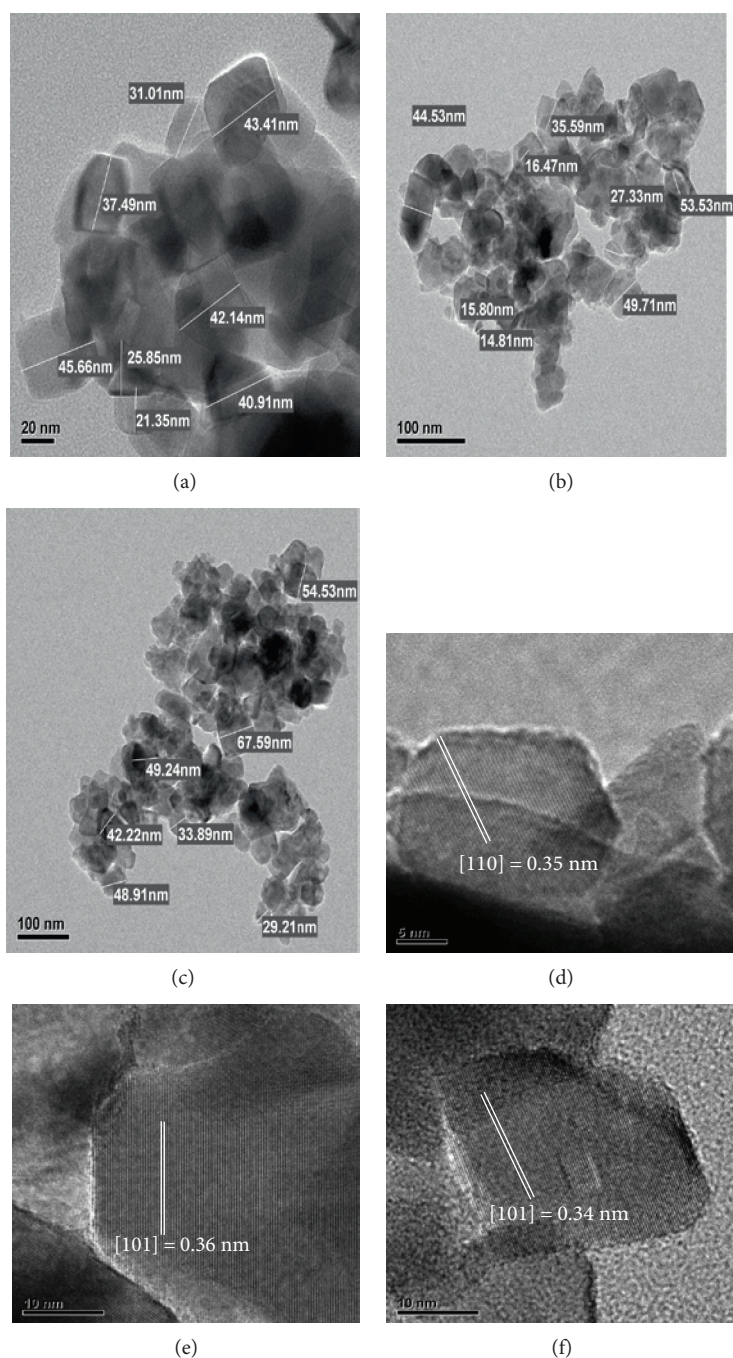


FIGURE 2: TEM images of (a)  $T_{\text{control}}$ , (b)  $(NS)_{0.06}\text{-}T_{\text{FA}}$ , and (c)  $(NS)_{0.06}\text{-}T_{\text{AA}}$ . Lattice fringes spacing of (d) [110] crystallographic plane of rutile in  $T_{\text{control}}$  and (e and f) [101] crystallographic plane of anatase in  $(NS)_{0.06}\text{-}T_{\text{FA}}$  and  $(NS)_{0.06}\text{-}T_{\text{AA}}$  photocatalyst powders, respectively.

in the supplementary information (Figure S1, Section S.1. available online at <https://doi.org/10.1155/2017/7268641>). Figures 3(a) and 3(b) also illustrate that no observable change in the intensity of the  $\text{COO}^-$  stretches were recorded with the addition and an increase in the dopant content, which means that the NS dopants assist in maintaining a strong  $\text{TiO}_2$  oligomer network. In support, a peak at  $2060\text{ cm}^{-1}$  in the samples  $((NS)_{0.1}\text{-}T_{\text{FA}}$  and  $(NS)_{0.1}\text{-}T_{\text{AA}}$ ) was developed, which is assumed to represent CN bonds [28].

Figure S2 (supplementary information) shows the IR spectra of samples  $(T_{\text{control}}, T_{\text{FA}}, (NS)_{0.08}\text{-}T_{\text{FA}}, T_{\text{AA}}, \text{ and } (NS)_{0.08}\text{-}T_{\text{AA}})$  calcined at  $700^\circ\text{C}$ . All the samples maintained the broad peak at  $3178\text{ cm}^{-1}$  attributed to OH groups, and the OH peak intensity increases due to carboxylic acid chelation and NS codoping which is a positive sign for enhanced photocatalysis. It is obvious that these hydroxyl ions are main hole scavengers resulting in the formation of hydroxyl radicals required for the degradation of organic pollutants.

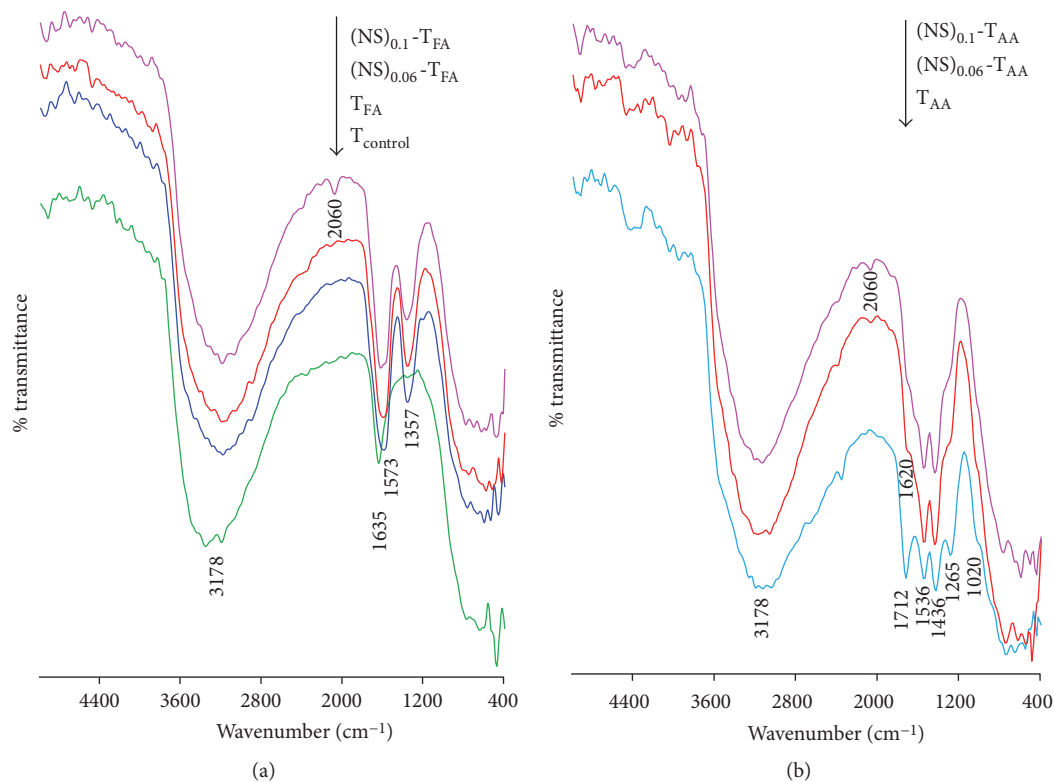


FIGURE 3: FTIR spectra of precalcined powders (a)  $T_{\text{control}}$ ,  $T_{\text{FA}}$ ,  $(\text{NS})_{0.06}\text{-}T_{\text{FA}}$ , and  $(\text{NS})_{0.1}\text{-}T_{\text{FA}}$  and (b)  $T_{\text{AA}}$ ,  $(\text{NS})_{0.06}\text{-}T_{\text{AA}}$ , and  $(\text{NS})_{0.1}\text{-}T_{\text{AA}}$ .

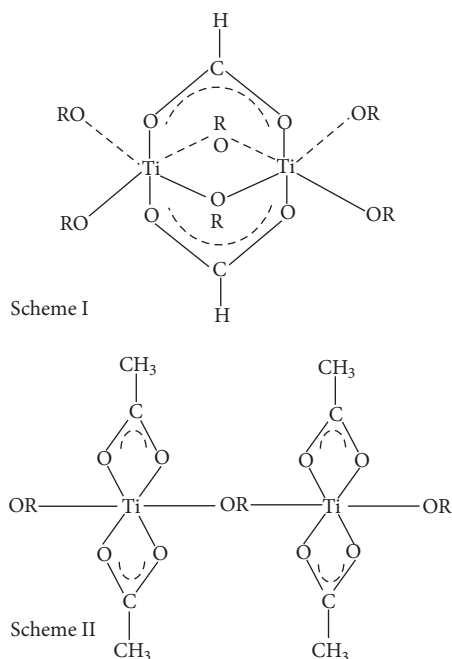


FIGURE 4: Proposed schemes of (I) formate group and (II) acetate group chelation with titanium precursor.

**3.3. Raman Spectroscopy.** Raman of the precalcined control and NS-codoped  $\text{TiO}_2$  powders was carried out to complement FTIR spectroscopy and XRD results. As shown in Figures 5(a) and 5(b), the presence of the peaks at  $146\text{ cm}^{-1}$

( $1\text{-E}_g$ ),  $392\text{ cm}^{-1}$  ( $A_{1g}$ ),  $512\text{ cm}^{-1}$  ( $B_{1g}$ ), and  $632\text{ cm}^{-1}$  ( $2\text{-E}_g$ ) in the Raman of modified  $\text{TiO}_2$  ( $T_{\text{FA}}$ ,  $T_{\text{AA}}$ ,  $(\text{NS})_{0.06}\text{-}T_{\text{FA}}$ ,  $(\text{NS})_{0.1}\text{-}T_{\text{FA}}$ ,  $(\text{NS})_{0.06}\text{-}T_{\text{AA}}$ , and  $(\text{NS})_{0.1}\text{-}T_{\text{AA}}$ ) is indicative of the four peak patterns that would be expected for anatase.

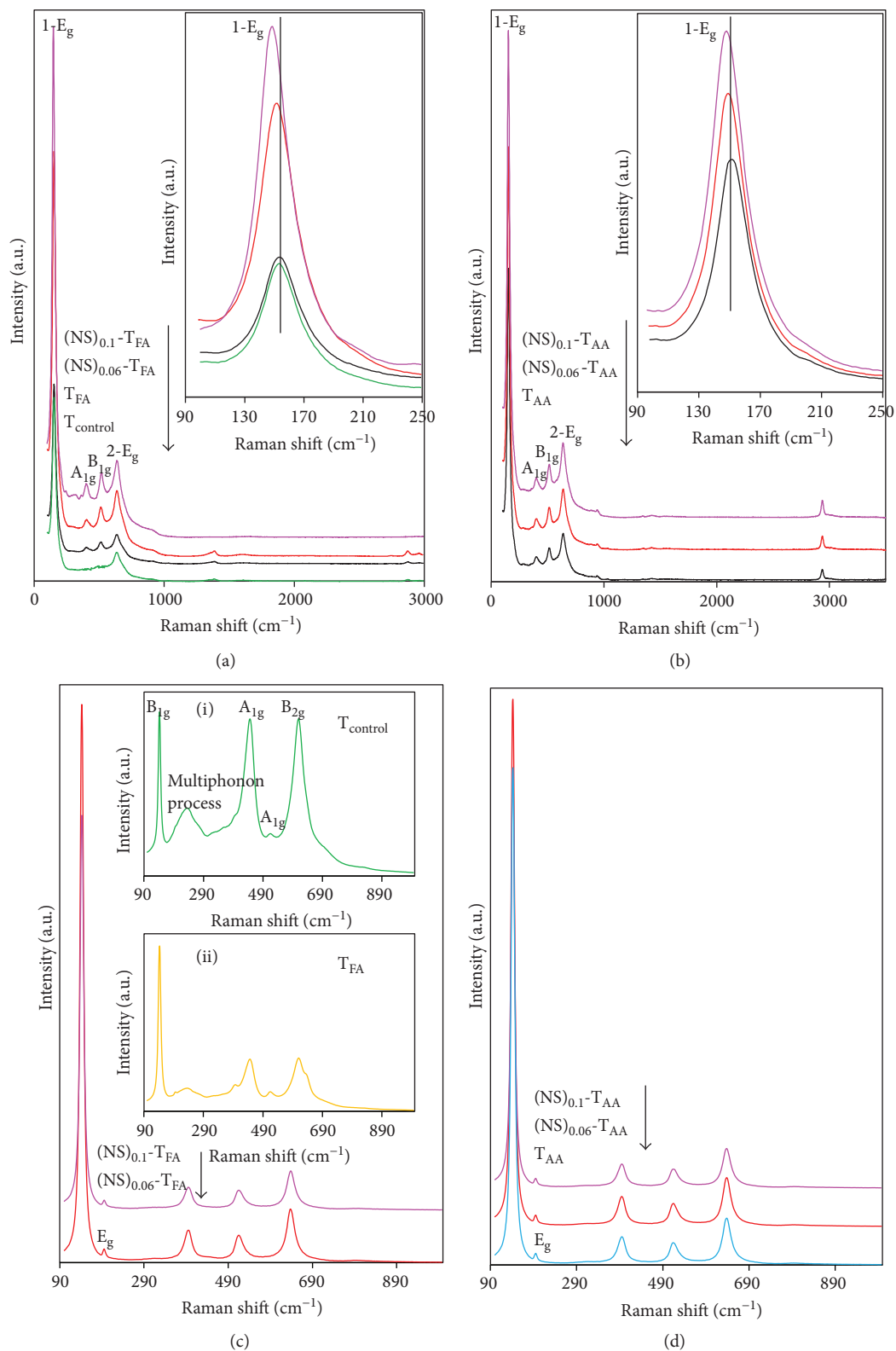


FIGURE 5: Raman spectra and 1-E<sub>g</sub> mode shifting (insert) of precalcined powders (a)  $T_{\text{control}}$ ,  $T_{\text{FA}}$ ,  $(\text{NS})_{0.06}\text{-}T_{\text{FA}}$ , and  $(\text{NS})_{0.1}\text{-}T_{\text{FA}}$  and (b)  $T_{\text{AA}}$ ,  $(\text{NS})_{0.06}\text{-}T_{\text{AA}}$ , and  $(\text{NS})_{0.1}\text{-}T_{\text{AA}}$ . Raman spectra of the powders calcined at 700°C (c)  $(\text{NS})_{0.06}\text{-}T_{\text{FA}}$ ,  $(\text{NS})_{0.1}\text{-}T_{\text{FA}}$ ,  $T_{\text{control}}$  (insert (i)), and  $T_{\text{FA}}$  (insert (ii)) and (d)  $T_{\text{AA}}$ ,  $(\text{NS})_{0.06}\text{-}T_{\text{AA}}$ , and  $(\text{NS})_{0.1}\text{-}T_{\text{AA}}$ .

In comparison, the Raman spectrum of  $T_{\text{control}}$  (Figure 5(a)) showed just two peaks of distinctions which are at 146 and  $632\text{ cm}^{-1}$ . This result indicated that in the absence of carboxylic acid, the Ti-O atoms are randomly arranged as opposed to the more ordered structure shown in Figures 5(a) and 5(b) for the samples  $T_{\text{FA}}$  and  $T_{\text{AA}}$  where either formic acid or acetic acid was employed in the synthesis process as a chelating agent. As discussed earlier in the FTIR study, the use of NS dopants and an increase in their concentration do not induce a reduction in the intensity of carboxylate stretches. This indicates that titania formate or acetate complex is becoming stronger and results in the formation of a structurally strong oligomer that upon calcination easily formed a crystalline anatase  $\text{TiO}_2$ . This result is supported by the Raman analysis; evidently, it can be seen that the intensities of the respective anatase of four Raman peaks are increased and their widths are broadened after NS codoping. This shows that the stability of anatase is promoted and, in addition, after calcination, will result into well crystalline anatase particles with decreased particle size. To further elaborate the effect of the addition of dopants, the insert in Figures 5(a) and 5(b) shows the Raman band shift and broadening in the  $E_g$  mode ( $146\text{ cm}^{-1}$ ) of precalcined  $(\text{NS})_x\text{-}T_{\text{FA}}$  and  $(\text{NS})_x\text{-}T_{\text{AA}}$  (where  $x = 0.06$  and  $0.1$  mol%) powders compared to  $T_{\text{control}}$ ,  $T_{\text{FA}}$ , and  $T_{\text{AA}}$  samples, respectively. The anomalous variation in the intensities of the Raman band, shifting towards lower wavenumbers and broadening, obviously showed the effect of NS dopants indicating that dopants effect the titanium carboxylate complex before crystallization has occurred. This also assured that nitrogen substitutes for oxygen atoms and sulphur substitutes for titanium atoms in the titania lattice. In comparison to  $(\text{NS})_x\text{-}T_{\text{FA}}$ , the Raman spectra of  $(\text{NS})_x\text{-}T_{\text{AA}}$  (where  $x = 0, 0.06$ , and  $0.1$  mol%) powders (Figure 5(b)) showed a peak in the range  $2800\text{--}3000\text{ cm}^{-1}$  ascribed to OH stretches [24], whose intensity increases with NS amount. This result is supported by the FTIR analysis; as shown in Figure 3(b), a broad band at  $2800\text{--}3600\text{ cm}^{-1}$  is ascribed to the OH groups. This result further supports the formation of different modes of acetate and formate bonding with titanium as proposed previously (Figure 4).

Figures 5(c) and 5(d) show the Raman spectra of the powder calcined at  $700^\circ\text{C}$ . The insert (i) in Figure 5(c) is the Raman spectrum of  $T_{\text{control}}$  which obviously demonstrates the anatase-rutile structure; the rutile peaks are at  $141\text{ cm}^{-1}$  ( $B_{1g}$ ),  $235\text{ cm}^{-1}$  (multiphonon process),  $445\text{ cm}^{-1}$  ( $A_{1g}$ ), and  $608\text{ cm}^{-1}$  ( $B_{2g}$ ) while a low intensity peak is observed at  $512\text{ cm}^{-1}$  ( $A_{1g}$ ) which belongs to that of the anatase phase. The Raman analysis is ratified by the XRD results according to which the  $T_{\text{control}}$  sample is composed of anatase-rutile (1 : 99) mixture. The insert (ii) in Figure 5(c) is the Raman spectrum of  $T_{\text{FA}}$ ; the Raman modes stand for rutile at 141, 235, 445, and  $608\text{ cm}^{-1}$  whereas anatase peaks were recorded at 396 (weak emerging peak), 512, and  $636\text{ cm}^{-1}$  (a weak shoulder), respectively, which are in agreement with the XRD results which demonstrate that  $T_{\text{FA}}$  powder is a composite mixture of anatase-rutile in the proportion of 11 : 89. This result further illustrates that due to the formic acid chelation characteristic, anatase formation is favored;

the intensity of the rutile Raman peaks decreases while anatase Raman peaks are developing. The rest of the Raman spectra shown in Figure 5(c) designate that of  $(\text{NS})_{0.06}\text{-}T_{\text{FA}}$  and  $(\text{NS})_{0.1}\text{-}T_{\text{FA}}$  and those in Figure 5(d) are for  $(\text{NS})_x\text{-}T_{\text{AA}}$  (where  $x = 0, 0.06$ , and  $0.1$  mol%). The peaks ( $142, 197$  ( $E_g$ ),  $396, 516$ , and  $635\text{ cm}^{-1}$ ) recorded in all the Raman spectra stand for anatase phase.

**3.4. X-Ray Photoelectron Spectroscopy (XPS).** X-ray photoelectron spectroscopy analysis was performed to determine the chemical composition and to identify the chemical states of the elements present in the codoped  $\text{TiO}_2$ . In addition to the main peaks of titanium ( $\text{Ti}2p$ ,  $459.1\text{ eV}$ ), oxygen ( $\text{O}1s$ ,  $530.3\text{ eV}$ ), and carbon ( $\text{C}1s$ ,  $285.1\text{ eV}$ ), the XPS survey spectrum of  $(\text{NS})_{0.06}\text{-}T_{\text{FA}}$  sample clearly shows the peaks of the dopants nitrogen ( $\text{N}1s$ ,  $400.5\text{ eV}$ ) and sulphur ( $\text{S}2p$ ,  $169.2\text{ eV}$ ) compared to  $T_{\text{FA}}$  powder as shown in Figure 6. The enlarged view for the  $\text{N}1s$ ,  $\text{C}1s$ , and  $\text{S}2p$  peaks is also shown in Figure 6(a) insert. All the peaks were calibrated to the  $\text{C}1s$  peak which is attributed to the advantageous carbon from the XPS instrument itself and to the residual carbon from the precursor solution. The relative atomic percentage of the elements in the calcined powder ( $(\text{NS})_{0.06}\text{-}T_{\text{FA}}$ ) estimated from the XPS data were determined to be about 39.0, 52.7, 4.5, 1.8, and 2.0 at.% for titanium, oxygen, carbon, nitrogen, and sulphur, respectively.

The deconvoluted peaks of  $\text{Ti}2p$ ,  $\text{O}1s$ ,  $\text{N}1s$ , and  $\text{S}2p$  are shown in Figures 6(b), 6(c), 6(d), and 6(e). The  $\text{Ti}2p$  spectrum in Figure 6(b) shows two characteristic doublets for  $\text{Ti}2p_{3/2}$  at  $456.2$  and  $459.0\text{ eV}$  and for  $\text{Ti}2p_{1/2}$  at  $463$  and  $464.7\text{ eV}$ . The  $459.0$  and  $464.7$  is attributed to  $\text{Ti}^{4+}$  while  $456.2$  and  $463.2\text{ eV}$  is assigned to  $\text{Ti}^{3+}$  in  $\text{TiO}_2$ . The  $\text{O}1s$  spectrum shown in Figure 6(c) can be decomposed into four peaks, the binding energy at  $530.1\text{ eV}$  is attributed to crystal lattice oxygen ( $\text{Ti}^{4+}\text{-O}$ ), the peak at  $530.6\text{ eV}$  represents the oxygen in the  $\text{S-O-Ti}$  group, and the binding energy at  $531.4\text{ eV}$  is assigned to the  $\text{Ti}^{3+}\text{-O}$  group in  $\text{TiO}_2$  nanocomposite or to the  $\text{S-O-S}$  group while the surface hydroxyl ( $\text{O-H}$ ) groups are denoted by binding energy at  $532.6\text{ eV}$  [29]. The high-resolution spectrum of  $\text{N}1s$  shown in Figure 6(d) is divided into four peaks: the first peak at lower binding energy of  $399.1\text{ eV}$  is attributed to substitutional N in the  $\text{O-Ti-N}$  structure implying that lattice oxygen atoms are substituted by N atoms; the second and third peaks at  $400.4$  and  $401.6\text{ eV}$  are attributed to  $\text{Ti-N-O}$  and  $\text{Ti-O-N}$  bonds illustrating an interstitial N state in the codoped  $\text{TiO}_2$  powder; and the fourth peak at the higher binding energy of  $403.6\text{ eV}$  can be assigned to nitrogen species bound to various surface oxygen sites (such as  $\text{NO}$  or  $\text{NO}_2$ ) [30, 31]. Figure 6(e) shows the corresponding high-resolution spectrum of the  $\text{S}2p$  region; after deconvolution, the peak at  $168.5\text{ eV}$  is attributed to  $\text{S}^{4+}$  and the peak at  $169.0\text{ eV}$  is assigned to  $\text{S}^{6+}$ , suggesting that sulphur was incorporated into the  $\text{TiO}_2$  lattice via direct substitution of titanium atoms [32].

**3.5. UV-Vis Diffuse Reflectance Spectroscopy (UV-Vis DRS).** UV-vis diffuse absorption/reflectance measurements were recorded to investigate the light absorption characteristics of the prepared powders. Diffuse absorption spectra of the

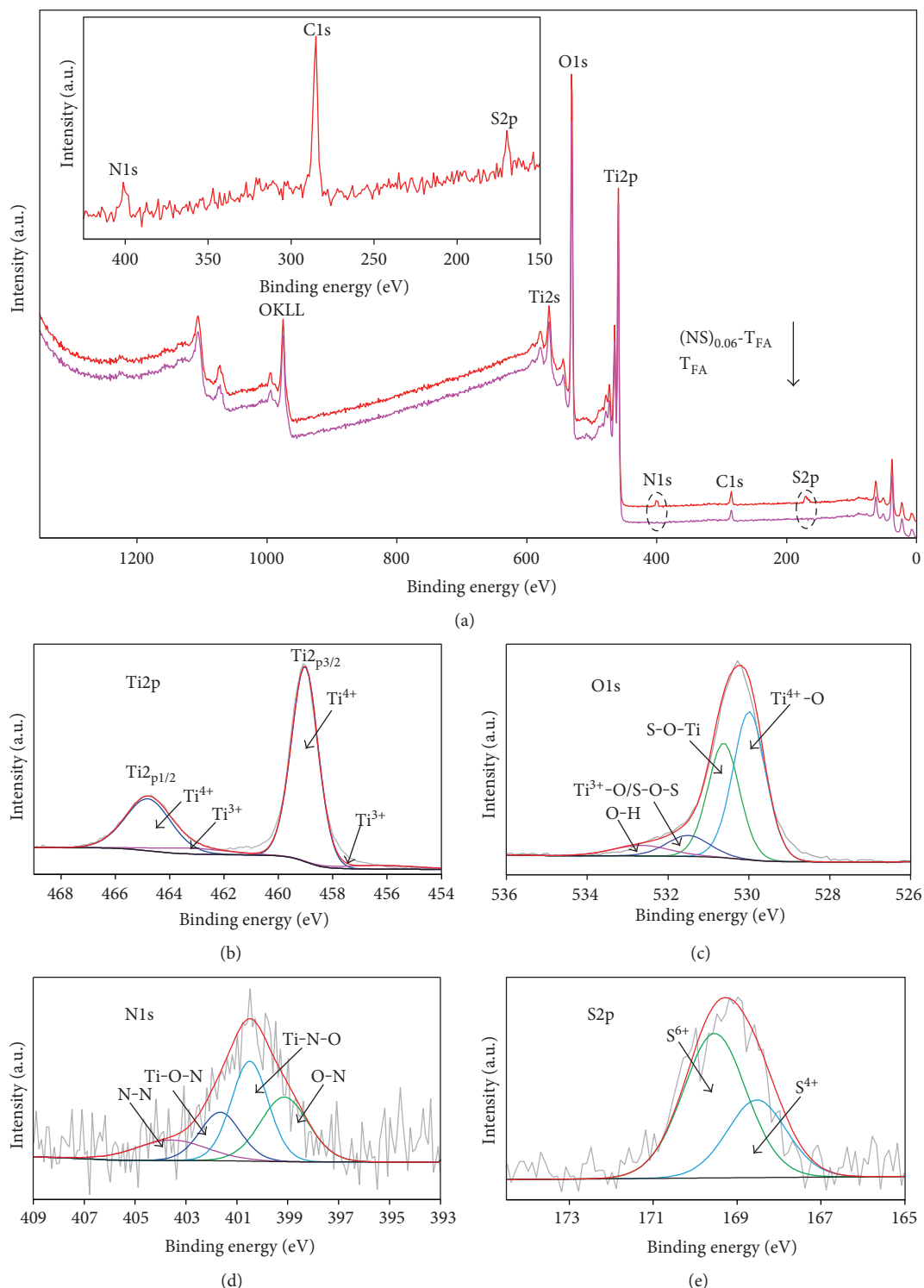


FIGURE 6: XPS spectra of  $(NS)_{0.06}\text{-T}_{FA}$  and  $T_{FA}$  powders. (a) Survey spectrum, insert (showing peaks for N1s, C1s, and S2p), (b) high-resolution spectrum of Ti2p, (c) high-resolution spectrum of O1s, (d) high-resolution spectrum of N1s, and (e) high-resolution spectrum of S2p.

powders ( $T_{FA}$ ,  $(NS)_{0.06}\text{-T}_{FA}$ ,  $T_{AA}$ , and  $(NS)_{0.06}\text{-T}_{AA}$ ) calcined at  $700^{\circ}\text{C}$  shown in Figure 7 clearly depict that codoped powders have a remarkable red shift absorption profile up to 470 nm, and the light absorption in the visible region indicates the successful insertion of the NS dopants into the  $TiO_2$  lattice as shown in the XPS results.

Nitrogen atoms can occupy either substitutional or interstitial sites within the  $TiO_2$  crystal lattice; published literature states that both types of nitrogen insertion lead to localized states in the  $TiO_2$  band gap which results in visible light absorption [22, 33]. In addition, it is also reported in the work of Ihara et al. [7] that oxygen vacancies produced by

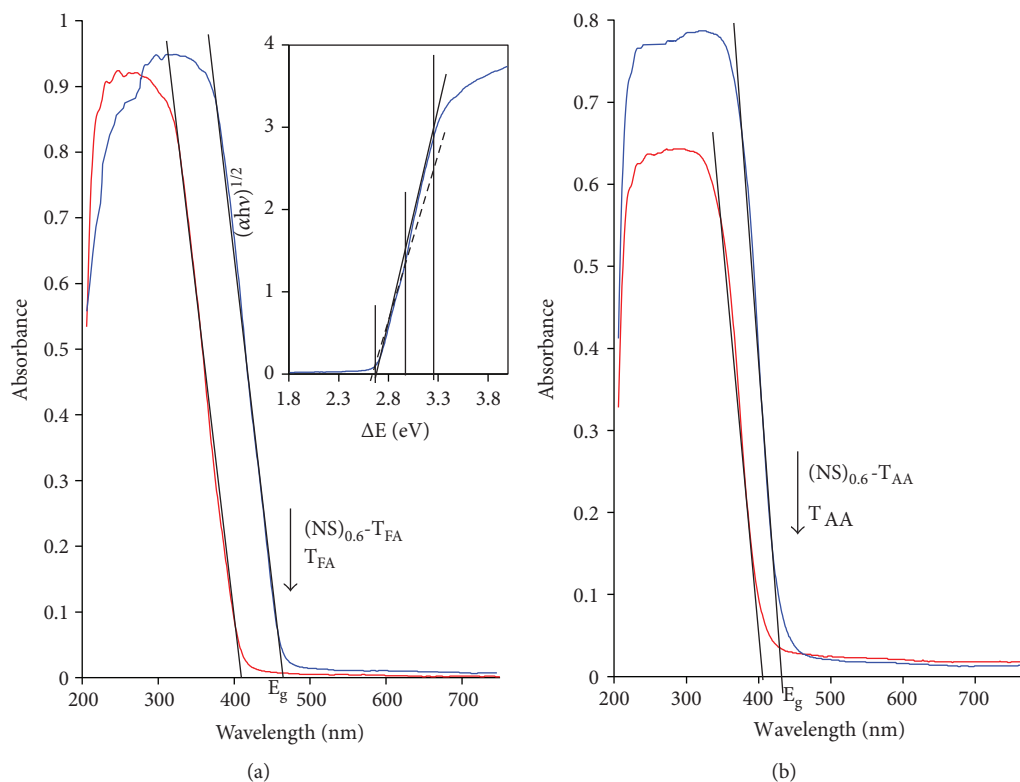


FIGURE 7: UV-vis DRS absorption spectra of (a)  $T_{FA}$ ,  $(NS)_{0.06}-T_{FA}$ , and Tauc plot of  $(NS)_{0.06}-T_{FA}$  powder (insert) and (b)  $T_{AA}$  and  $(NS)_{0.06}-T_{AA}$  powders were calcined at  $700^{\circ}\text{C}$ .

N-doping can induce visible light responses. Nitrogen has a lower valency state than oxygen; thus, for charge equilibrium in doped  $\text{TiO}_2$ , oxygen vacancies are promoted. Our PL analysis showed oxygen vacancies (F,  $F^+$  centers) at 460, 466, and at 610 nm (Figure S3 and Table S1, supplementary information Section S.2.); Li et al. [34] stated that F and  $F^+$  centers are situated at 2.7 and 2.4 eV from the valence band, while Cronemeyer [35] reported that oxygen vacancy states existed at 0.75–1.18 eV below the conduction band minimum of  $\text{TiO}_2$ . Electrons can be excited from the valence band to the oxygen vacancies (F,  $F^+$ , and  $F^{++}$ ) centers followed by transition to the conduction band of  $\text{TiO}_2$ ; thus, band narrowing due to the F,  $F^+$ , and  $F^{++}$  centers caused by N-doping cannot be neglected.

Doping of sulphur into the  $\text{TiO}_2$  lattice also helps in the band gap narrowing of  $\text{TiO}_2$ , because sulphur atoms can alter  $\text{TiO}_2$  conduction or valence band (or both of them) by producing impurity levels in the band gap of  $\text{TiO}_2$  as a consequence improving the visible light absorption [29]. Ma et al. [36] reported that visible light absorption in S-doped  $\text{TiO}_2$  can be attributed to the formation of O-Ti-S or Ti-O-S bonds, which could lead partial electron transfers from sulphur atoms to titanium and oxygen atoms.

Figure 7 and Table 1 illustrate that narrowing of the band gap in  $T_{FA}$  and  $(NS)_x-T_{FA}$  is more than that in  $T_{AA}$  and  $(NS)_x-T_{AA}$  samples; two absorption onsets were recorded in  $(NS)_x-T_{FA}$  samples (Figure 7(a) insert, Tauc plot of  $(NS)_{0.06}-T_{FA}$  powder): a long absorption tail gives the value of 2.75 eV (denoted by full line) and the small absorption tail

gives the value of 2.68 eV (denoted by dotted line). The cut-off energy values are measured by extrapolating the linear portion of the spectrum until it intersects the  $h\nu$  axis ( $x$ -axis) at  $E_g$ . The presence of the small absorption tail indicates the substitutional doping of nitrogen replacing the oxygen atoms in the  $\text{TiO}_2$  lattice; as a result, an impurity band (mixing of N2p states with O2p states) is formed above the valence band of  $\text{TiO}_2$ . While the long absorption tail in  $(NS)_x-T_{FA}$  and in  $(NS)_x-T_{AA}$  samples is attributed to both, institutional doping of nitrogen atoms into the  $\text{TiO}_2$  lattice results in forming an isolated N impurity level above the valence band and mixing of S states with the conduction band (Ti3d). Therefore, the visible light response in NS-codoped  $\text{TiO}_2$  powder may be ascribed to the combination of isolated N impurity levels and impurity levels due to mixing of the N states and S states with valence band O2p and Ti3d states, respectively. In addition, the formation of  $\text{Ti}^{3+}$  centers and oxygen vacancies as depicted in XPS and PL studies may also help to improve the visible light absorption. Comparing the Tauc plot and absorption spectra of  $(NS)_x-T_{FA}$  powders to the  $(NS)_x-T_{AA}$  powders, the second small absorption tail is absent in the latter and this behaviour may be assigned to the difference in the chelating linkages of the two carboxylic acids. Furthermore, a blue shift in absorption spectrum of  $(NS)_x-T_{FA}$  and  $(NS)_x-T_{AA}$  powders was noticed on the increase in dopant content beyond 0.06 and 0.08 mol%, respectively. This is due to the decrease in the rutile fraction within the sample, and probably,

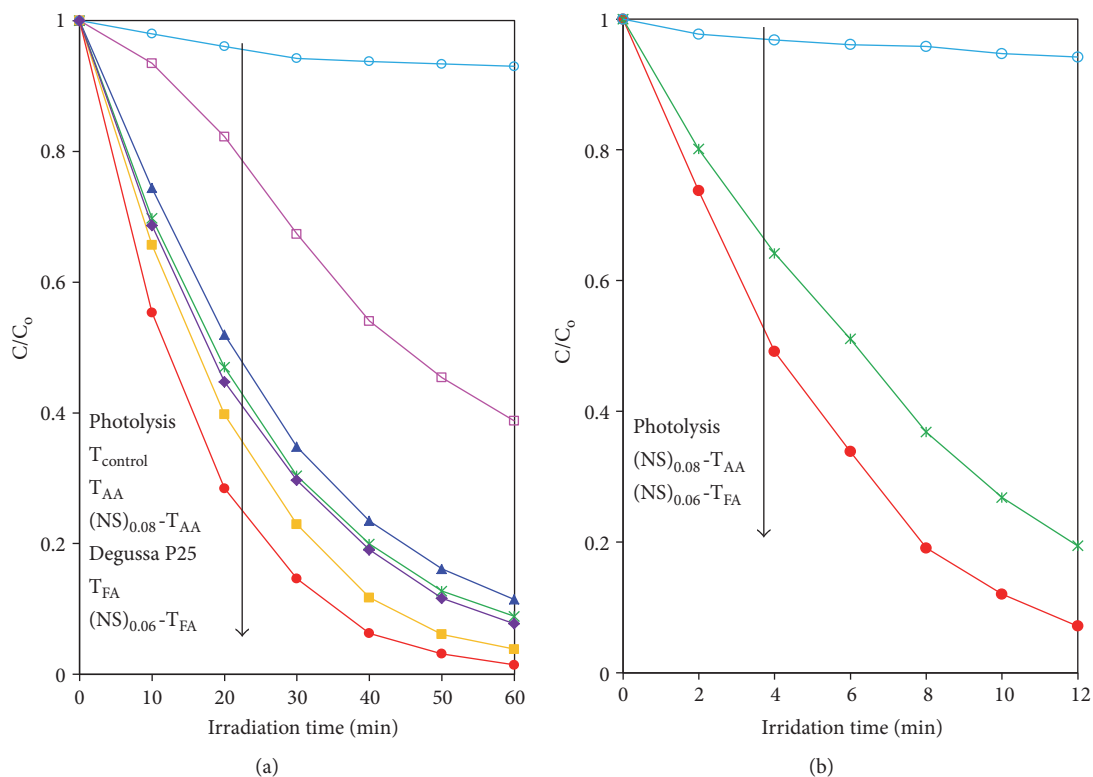


FIGURE 8: Photolytic and photocatalytic activity curves of 4-chlorophenol degradation under (a) UV irradiation and (b) visible irradiation for Degussa P25 and the selected photocatalyst powders calcined at 700°C.

the dopants exceed their solubility limit in  $TiO_2$ , which diffuse to accumulate in the grain boundaries without contributing to the narrowing in the  $TiO_2$  band gap [23]. Thus, an optimum amount of dopant addition in  $TiO_2$  will bring the desired improvement in visible light characteristics of  $TiO_2$ ; beyond such limit, further dopant addition will contribute towards the absorption blue shift.

**3.6. Photocatalytic Activity.** The UV and visible light photocatalytic activities of the control, commercially available Degussa P25 and NS-codoped  $TiO_2$  powders, in addition to the effect of photolysis (absence of photocatalyst) were studied by monitoring the degradation of 4-chlorophenol (4-CP) as a model pollutant; the obtained results were shown in Figure 8. The UV activity trend presented in Figure 8(a) was as follows:  $(NS)_{0.06}-T_{FA} > T_{FA} > Degussa\ P25 \approx (NS)_{0.08}-T_{AA} > T_{AA} > T_{control}$ . Similarly, in visible light irradiation (Figure 8(b)), the  $(NS)_{0.06}-T_{FA}$  photocatalyst also showed higher activity than the  $(NS)_{0.08}-T_{AA}$  sample. It should be noted that the  $(NS)_{0.08}-T_{AA}$  powder has the highest activity among the  $(NS)_x-T_{AA}$  (where  $x$  is 0.02, 0.04, 0.06, and 0.1 mol% dopant concentration) and  $T_{AA}$  samples. In the visible activity experiments, no results were presented for the control  $TiO_2$  and Degussa P25 catalysts as they absorb light mainly in the UV region due to their high band gap value and they are not suitable for visible light photocatalysis. Moreover, experimentally (Figure 8(a)), it was observed that the degradation of the model pollutant 4-CP was not affected by applying direct UV and or visible light in the absence of

photocatalyst (photolysis). This means that any change in the pollutant concentration can be ascribed only to the photocatalysis [21].

The highest photocatalytic activity of  $(NS)_{0.06}-T_{FA}$  powder can be ascribed to several reasons such as the composite nature of the sample (anatase/rutile), surface hydroxyl ions, narrowed band gaps, the enhanced formation of  $Ti^{3+}$  centers, and oxygen vacancies due to NS codoping. As a result of synergistic effects between anatase-rutile and the charge trapping of dopant ions, the electron-hole recombination is decreased, and as a consequence, the charge carriers are diffused to the surface to be consumed in the process redox reactions. FTIR studies showed that as a result of chelation and NS codoping in  $TiO_2$ , the surface hydroxyl groups (a broad absorption band ( $2800-3600\text{ cm}^{-1}$ ) centered at  $3178\text{ cm}^{-1}$ ) are intact even at the high calcination temperatures of 700°C. These hydroxyl groups are very significant for the enhanced activity because they act as scavengers for the photogenerated holes to produce hydroxyl radicals which react with the organic compounds for their degradation. Doped powders have lower band gap values compared to control powders and thus are capable to be irradiated with longer wavelength light to produce exciton pairs that result in the increased production of super oxide anions ( $O_2^{\bullet-}$ ) and hydroxyl radicals ( $OH^{\bullet}$ ); these radicals then take part in pollutant decomposition. Moreover, due to charge compensation, NS codoping promotes the formation of oxygen vacancies. During photocatalytic processes, these oxygen vacancies not only promote photocatalyst absorption for

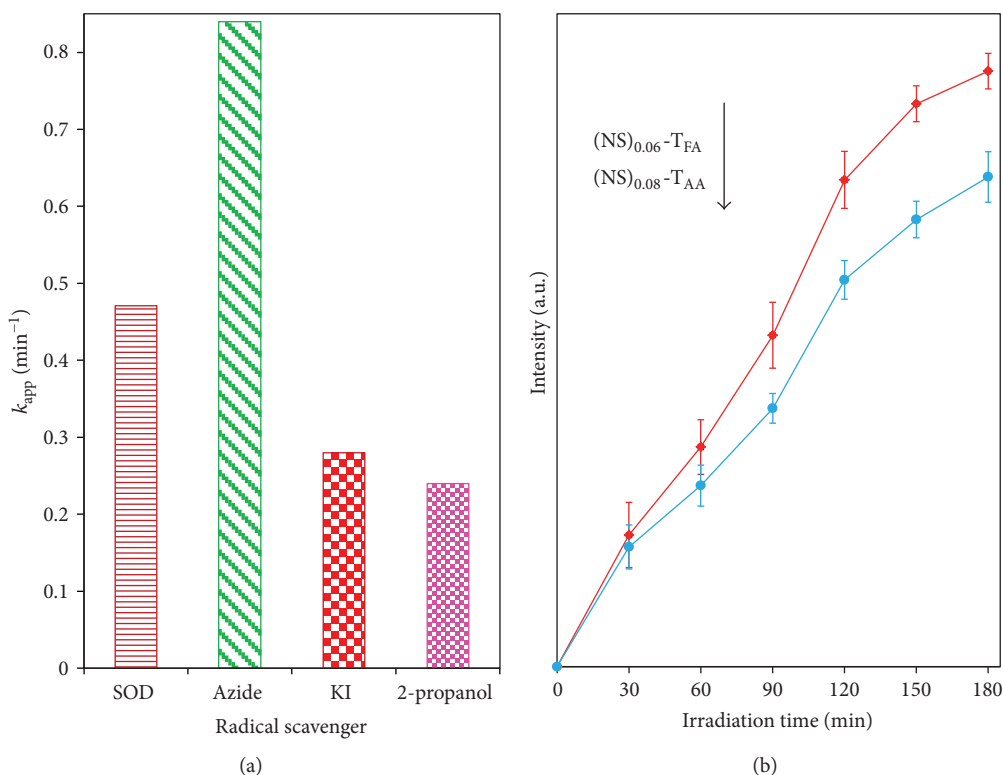


FIGURE 9: (a) Apparent first-order constant ( $k_{app}$ ) for the degradation of 4-CP ( $0.007 \text{ g}\cdot\text{l}^{-1}$ ) by  $(NS)_{0.06}\text{-T}_{FA}$  photocatalyst using different radical scavengers and (b) change in PL intensity of the highly active photocatalyst powders dispersed TA solution under UV illumination.

the lower energy photons but also acts as an active site for the formation of active species ( $\text{O}_2^{\bullet-}$  and  $\text{OH}^\bullet$  radicals) required for the photocatalytic reactions [34, 37].

Figure S4 (supplementary information) shows the pseudo-first-order kinetics of 4-chlorophenol degradation; under UV irradiations (Figure S4a), the apparent rate constants,  $k_{app}$  values (obtained from the slope of the plot  $-\ln(C/C_0)$  versus irradiation time), for the powders  $T_{control}$ ,  $T_{FA}$ ,  $T_{AA}$ ,  $(NS)_{0.06}\text{-T}_{FA}$ , and  $(NS)_{0.06}\text{-T}_{AA}$  are 0.01, 0.05, 0.04, 0.07, and 0.04  $\text{min}^{-1}$ , respectively. This shows that  $(NS)_{0.06}\text{-T}_{FA}$  powder has high activity among the prepared samples, and its rate constant value of  $0.07 \text{ min}^{-1}$  is nearly 1.4 times higher than  $T_{FA}$  and 2.5 times higher than  $T_{control}$  powders. Also, under visible light irradiations (Figure S4b), the sample  $NS_{0.06}\text{-T}_{FA}$  showed a rate constant value of  $0.22 \text{ min}^{-1}$  which is nearly 1.6 times higher than  $(NS)_{0.08}\text{-T}_{AA}$  powder which showed the highest activity among the doped powders employing acetic acid in the photocatalyst synthesis process.

**3.7. Role of Radical Scavenger.**  $\text{TiO}_2$  photocatalysis involves a complex interdependent series of chemical reactions and a number of different reactive oxidizing species (ROS). In an attempt to assess the role of the different associated ROS, several scavenger agents were used during the photocatalytic tests of the model 4-chlorophenol pollutant. It is obvious that oxygen plays a significant role in  $\text{TiO}_2$  photocatalysis, because it acts as an electron scavenger to inhibit recombination of hole/electron pairs, thus initiating oxidative reaction

such as the formation of hydroxyl radicals ( $\text{OH}^\bullet$ ). As a result of this reaction, superoxide anion radicals ( $\text{O}_2^{\bullet-}$ ) are produced which have the potential to react directly by oxidative pathways, and it can also produce singlet oxygen or decompose to hydrogen peroxide ( $\text{H}_2\text{O}_2$ ), which is transferred to hydroxyl radicals during the photocatalytic process. To elucidate the formation of  $\text{O}_2^{\bullet-}$  species, the scavenger superoxide dismutase (SOD) is added to the solution ( $\text{SOD}_{red} + \text{O}_2^{\bullet-} + 2\text{H}^+ \rightarrow \text{SOD} + \text{H}_2\text{O}_2$ ) [38], which resulted in a decrease of 40% in the degradation rate of 4-CP under our experimental conditions (Figure 9(a)). To test the formation of singlet oxygen during the photocatalytic process, the scavenger azide was added to the solution ( $\text{O}^1 + \text{N}_3^- \rightarrow \bullet\text{N}_3 + \text{O}_2^{\bullet-}$ ) [39], which showed a decrease of 6% in the photodegradation rate; this result illustrates that singlet oxygen do not play a significant role in the degradation of 4-CP using  $(NS)_{0.06}\text{-T}_{FA}$  as a photocatalyst. Photoillumination of  $\text{TiO}_2$  leads to the production of holes, which can react with adsorbed  $\text{H}_2\text{O}$  to yield hydroxyl radicals ( $\text{OH}^\bullet$ ) on the catalyst surface. The scavengers potassium iodide (KI) and 2-propanol were used to measure the participation of holes and hydroxyl radicals in the photocatalytic process [40]; the result showed that the degradation rate decreased about 60 and 63%, respectively. In conclusion, these results showed that primarily holes and hydroxyl radicals followed by  $\text{O}_2^{\bullet-}$  species were mainly responsible for the degradation of 4-CP. To further support the production of major reactive species, the hydroxyl radicals were monitored by the PL method using terephthalic acid (TA) as the

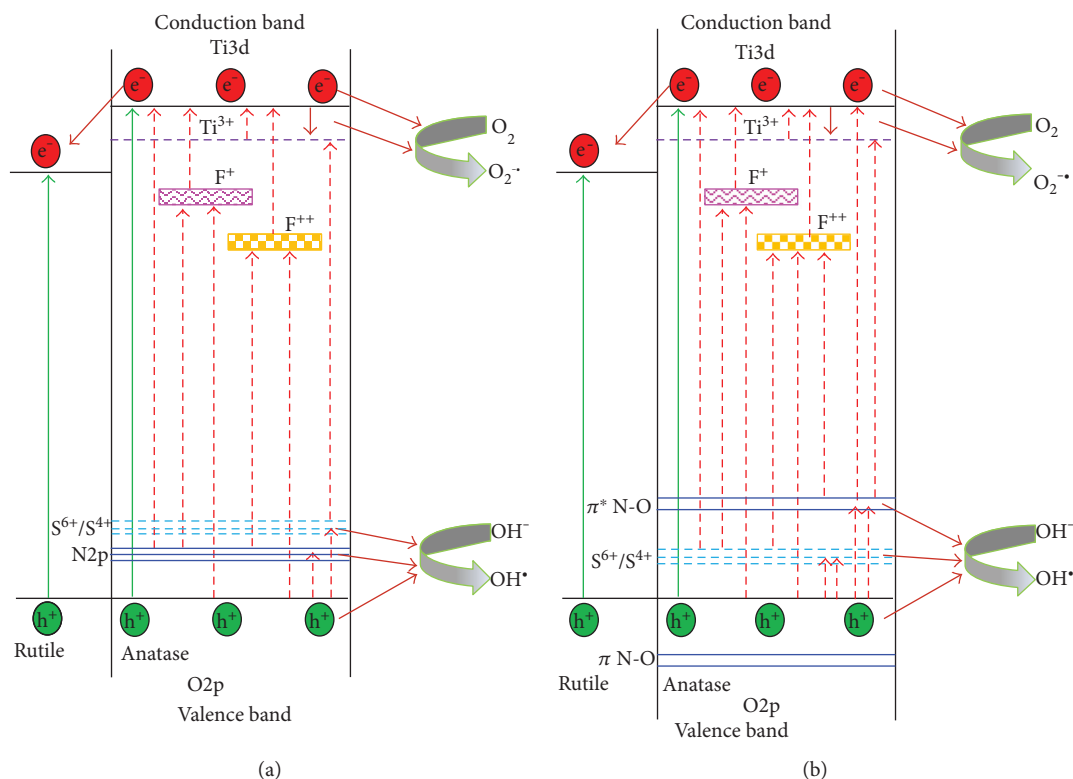


FIGURE 10: Mechanistic transfer pathways of charge carriers in NS-codoped powders under UV and visible light irradiations (a) substitutional doping of nitrogen and sulphur and (b) substitutional doping of sulphur and interstitial doping of nitrogen.

fluorescence probe in the aqueous solution [21]. TA reacts easily with hydroxyl radicals to produce the highly fluorescent 2-hydroxy terephthalic acid ( $TA + OH^\bullet \rightarrow TAOH$ ). Figure 9(b) shows the TAOH fluorescence intensity in the suspension solution with the highly active synthesized photocatalyst powder as a function of UV illumination time. It can be observed that the  $(NS)_{0.06}\text{-}T_{FA}$  powder produced a large amount of hydroxyl radicals compared to  $(NS)_{0.08}\text{-}T_{AA}$ , which is in agreement with the photocatalytic activity results shown in Figure 8. This result also indicates that a gain in the light absorption due to the decrease in the band gap of NS-doped powders helps the photoinduced carriers for producing hydroxyl radicals, which results in the enhanced degradation of 4-chlorophenol.

**3.8. Mechanistic Study.** In reference to the observed characterization and the UV-vis photocatalytic activity results, a probable mechanism explaining the transfer pathways of photogenerated charge carriers for the photodegradation of 4-chlorophenol is illustrated in Figure 10. The UV excitation of electrons from the valence band (VB) to the conduction band (CB) of  $TiO_2$  is denoted by full bold lines while that of visible light is represented by the bold dashed lines.

The enhanced UV-vis photocatalytic activity for the degradation of 4-CP was achieved with  $(NS)_{0.06}\text{-}T_{FA}$  and  $(NS)_{0.08}\text{-}T_{AA}$  catalyst powders. The  $(NS)_{0.06}\text{-}T_{FA}$  sample consists of anatase-rutile; due to the synergistic effect, there is enhanced separation between the photoinduced electrons and holes, since the CB of rutile is slightly lower than that

of anatase; thus, electrons in the anatase CB would immediately diffuse into the CB of rutile. Subsequently, the CB electrons react with the surface adsorbed oxygen molecules to produce superoxide anion radicals ( $O_2^{\bullet-}$ ), which are consumed in the degradation of 4-CP.

DRS spectra showed that incorporation of NS dopants in the  $TiO_2$  lattice through substitutional or interstitial doping can modify the  $TiO_2$  electronic band gap. The Tauc plot of  $(NS)_x\text{-}T_{FA}$  powders showed two diffused reflection onsets in comparison to  $(NS)_x\text{-}T_{AA}$  powders. The small absorption tail is attributed to the substitutional doping of nitrogen in the  $TiO_2$  lattice; as a result of substitutional N doping, occupied N2p-localized states (Figure 10(a)) appear above the O2p valence band, which narrows the band gap of  $TiO_2$  and shifts the optical absorption edge to the visible light region [33]. Electrons can be excited from this occupied N2p impurity level to the surface defect (oxygen vacancies and  $Ti^{3+}$  species) states and to  $TiO_2$  CB band under visible light irradiation. The long absorption tail is ascribed to the interstitial doping of nitrogen and mixing of S states with conduction band ( $Ti3d$ ) into  $TiO_2$ . With interstitial N doping, localized states with  $\pi$  character are generated by the NO bond [33]. Two antibonding states ( $\pi\text{-NO}$ ) lie above the O2p band and two deep energy bonding states ( $\pi^*\text{-NO}$ ) lie below the O2p states. It is the antibonding NO orbitals that facilitate visible light absorption as electrons can be excited from this occupied high energy state to the CB (Figure 9(b)). Moreover, some researchers believe that the interstitial N impurity which lies above the valence band may also act as a strong trapping site

for the photogenerated holes [41] and as a consequence helps to decrease the charge carriers recombination rate.

The S dopant may also induce an impurity level ( $S^{6+}/S^{4+}$ ) near the  $TiO_2$  CB band which not only helps in the decrease of  $TiO_2$  band gap but also helps to enhance production of electrons under visible light irradiations. Moreover, the N-impurity level may also behave as a trapping site for the VB holes like the S impurity level (Figure 10(a)) acts for the CB electrons; as a result, they inhibit the recombination of photoinduced holes and electrons.

PL (supplementary information Section S.2.) and XPS analyses verify the presence of  $Ti^{3+}$  centers and oxygen vacancies (F,  $F^+$ ), which contributed to the low energy photon absorption in doped  $TiO_2$ . Excess electrons in the CB or electrons excited from the valence band can cause the reduction of  $Ti^{4+}$  species to produce  $Ti^{3+}$  species in the bulk. These  $Ti^{3+}$  centers lie below the bottom of the CB and may act as trapping sites for visible light photoexcited electrons; afterwards, the trapped electrons are diffused to the surface for the production of superoxide anions ( $O_2^{\bullet-}$ ). Oxygen vacancy states introduced by doping into the  $TiO_2$  lattice may act as twofold: firstly, by inducing the visible light absorption, as a result, electrons from the oxygen vacancy states (F,  $F^+$ ), are excited to CB or to  $Ti^{3+}$  centers, and secondly, the oxygen vacancies can trap the photoinduced VB electrons and act as reactive centers for the photocatalytic process [30].

Thus, it is believed that S and N impurity levels,  $\pi^*$ -NO localized states, and  $Ti^{3+}$  centers and oxygen vacancies act cooperatively to narrow the NS  $TiO_2$  band gap, resulting in the visible light activity of NS- $TiO_2$ . As shown in Figure 10, the CB electrons or the electrons trapped at the sulphur impurity level react with surface-absorbed oxygen molecules to produce  $O_2^{\bullet-}$  species, while the VB holes or the holes trapped at the nitrogen impurity level react with hydroxyl groups ( $OH^-$ ) to produce hydroxyl radicals ( $OH^\bullet$ ). Afterwards, these radicals ( $O_2^{\bullet-}$ ,  $OH^\bullet$ ) take part in the degradation of organic pollutants under UV-vis light irradiations.

## 4. Conclusions

A systematic study was conducted to address the chelation of formic acid and acetic acid to the alkoxide precursor, and the effect of NS dopants on the physicochemical properties of carboxylic acid-modified  $TiO_2$  and on the anatase to rutile transformation temperature was performed. XRD studies showed that the formic and acetic acid-modified  $TiO_2$  samples were composed of a composite mixture of anatase-rutile phases and of a pure anatase phase, respectively, which was due to carboxylic acid chelation as evidenced by FTIR studies. In contrast, due to the absence of carboxylate linkages, the  $T_{control}$  sample was consisted of mainly rutile (99.0 wt.%) phase. Greater visible absorbance for the  $(NS)_x-T_{FA}$  samples were measured compared to  $(NS)_x-T_{AA}$  due to the different carboxylate coordination with titanium atoms; this means that nitrogen and sulphur atoms are doped substitutionally in formic acid-modified  $TiO_2$  with ease and in greater amounts compared to acetate-modified  $TiO_2$ . When evaluating the photocatalytic performance of the prepared samples, the  $(NS)_{0.06}-T_{FA}$  powder showed the highest activity

for the degradation of 4-chlorophenol under both UV and visible light irradiation. This enhanced photoactivity was attributed to the composite nature of the sample (anatase/rutile), photogenerated holes and surface hydroxyl ions, the narrowed band gap, formation of  $Ti^{3+}$  centers, and oxygen vacancies due to NS codoping. Finally, to verify the importance of the different reactive oxidizing species (ROS) involved in the photocatalytic process, some scavenger agents were employed, and the results showed that photogenerated holes,  $OH^\bullet$  radicals, and  $O_2^{\bullet-}$  species were primarily responsible for the degradation of 4-CP. In conclusion, this study will indeed offer more opportunities to investigate other chelating compounds with titanium precursors and the effect of metals (alkali, transition, and rare earth metals) and nonmetals on the chelation and physicochemical and photocatalytic properties of the final  $TiO_2$  material.

## Abbreviations

ART:	Anatase to rutile transformation
DFT:	Density functional theory
eV:	Electron volt
$\Delta$ :	The difference in asymmetric ( $\nu(COO^-)$ as) and symmetric carboxylate ( $-\nu(COO^-)$ s) stretches
$k_{app}$ :	Apparent rate constant
CB:	Conduction band
VB:	Valence band
UV:	Ultraviolet
Cu:	Copper
ROS:	Reactive oxidizing species
FWHM:	Full width at half maximum
$h\nu$ :	Photon energy
$\lambda$ :	Wavelength
$^\circ C$ :	Degree centigrade
$OH^\bullet$ :	Hydroxyl radicals
$O_2^{\bullet-}$ :	Superoxide anions
nm:	Nanometer
cm:	Centimeter
at. %:	Atomic percent.

## Conflicts of Interest

The authors declare that there is no conflict of interests regarding the publication of this paper.

## Acknowledgments

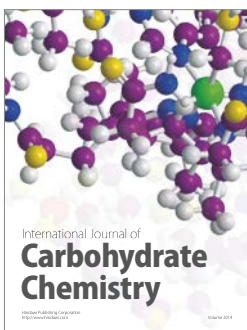
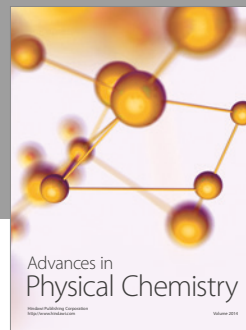
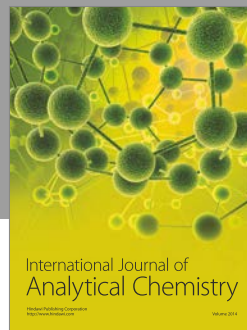
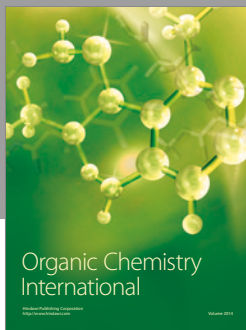
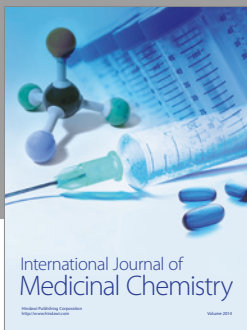
The authors would like to acknowledge the Natural Sciences and Engineering Research Council of Canada (NSERC) and the University of Engineering and Technology, Peshawar for providing support for this research.

## References

- [1] Y. Q. Wang, X. J. Yu, and D. Z. Sun, "Synthesis, characterization, and photocatalytic activity of  $TiO_{2-x}N_x$  nanocatalyst," *Journal of Hazardous Materials*, vol. 144, no. 1-2, pp. 328-333, 2007.
- [2] N. T. Nolan, M. K. Seery, S. J. Hinder, L. F. Healy, and S. C. Pillai, "A systematic study of the effect of silver on the chelation of formic acid to a titanium precursor and

- the resulting effect on the anatase to rutile transformation of TiO<sub>2</sub>,” *The Journal of Physical Chemistry C*, vol. 114, no. 30, pp. 13026–13034, 2010.
- [3] H. Zhao, L. Liu, J. M. Andino, and Y. Li, “Bicrystalline TiO<sub>2</sub> with controllable anatase-brookite phase content for enhanced CO<sub>2</sub> photoreduction to fuels,” *Journal of Materials Chemistry A*, vol. 1, no. 28, pp. 8209–8216, 2013.
  - [4] A. D. Paola, M. Bellardita, and L. Palmisano, “Brookite, the least known TiO<sub>2</sub> photocatalyst,” *Catalysts*, vol. 3, no. 1, pp. 36–73, 2013.
  - [5] D. Reyes-Coronado, G. Rodríguez-Gattorno, M. E. Espinosa-Pesqueira, C. Cab, R. de Coss, and G. Oskam, “Phase-pure TiO<sub>2</sub> nanoparticles: anatase, brookite and rutile,” *Nanotechnology*, vol. 19, no. 14, pp. 145605–14515, 2008.
  - [6] R. Asahi, T. Morikawa, T. Ohwaki, K. Aoki, and Y. Taga, “Visible-light photocatalysis in nitrogen-doped titanium oxides,” *Science*, vol. 293, no. 5528, pp. 269–271, 2001.
  - [7] T. Ihara, M. Miyoshi, Y. Iriyama, O. Matsumoto, and S. Sugihara, “Visible-light-active titanium oxide photocatalyst realized by an oxygen-deficient structure and by nitrogen doping,” *Applied Catalysis B: Environmental*, vol. 42, no. 4, pp. 403–409, 2003.
  - [8] H. Irie, Y. Watanabe, and K. Hashimoto, “Nitrogen-concentration dependence on photocatalytic activity of TiO<sub>2-x</sub>N<sub>x</sub> powders,” *The Journal of Physical Chemistry B*, vol. 107, no. 23, pp. 5483–5486, 2003.
  - [9] Y. Cong, J. Zhang, F. Chen, and M. Anpo, “Synthesis and characterization of nitrogen-doped TiO<sub>2</sub> nanophotocatalyst with high visible light activity,” *The Journal of Physical Chemistry C*, vol. 111, no. 19, pp. 6976–6982, 2007.
  - [10] T. Ohno, T. Mitsui, and M. Matsumura, “Photocatalytic activity of S-doped TiO<sub>2</sub> photocatalyst under visible light,” *Chemistry Letters*, vol. 32, no. 4, pp. 364–365, 2003.
  - [11] L. Szatmary, S. Bakardjieva, J. Subrt et al., “Sulphur doped nanoparticles of TiO<sub>2</sub>,” *Catalysis Today*, vol. 161, no. 1, pp. 23–28, 2011.
  - [12] R. G. Chaudhuri and S. Paria, “Visible light induced photocatalytic activity of sulfur doped hollow TiO<sub>2</sub> nanoparticles, synthesized via a novel route,” *Dalton Transactions*, vol. 43, no. 14, pp. 5526–5534, 2014.
  - [13] E. M. Rockafellow, L. K. Stewart, and W. S. Jenks, “Is sulfur doped TiO<sub>2</sub> an effective visible light photocatalyst for remediation,” *Applied Catalysis B: Environmental*, vol. 91, no. 1–2, pp. 554–562, 2009.
  - [14] P. Dong, B. Liu, Y. Wang, H. Pei, and S. Yin, “Enhanced photocatalytic activity of (Mo, C)-codoped anatase TiO<sub>2</sub> nanoparticles for degradation of methyl orange under simulated solar irradiation,” *Journal of Materials Research*, vol. 25, no. 12, pp. 2392–2400, 2010.
  - [15] H. Khan and D. Berk, “Characterization and mechanistic study of Mo<sup>6+</sup> and V<sup>5+</sup> codoped TiO<sub>2</sub> as a photocatalyst,” *Journal of Photochemistry and Photobiology A: Chemistry*, vol. 294, pp. 96–109, 2014.
  - [16] P. Periyat, D. E. McCormack, S. J. Hinder, and S. C. Pillai, “One-pot synthesis of anionic (nitrogen) and cationic (sulfur) codoped high temperature stable, visible light active, anatase photocatalysts,” *The Journal of Physical Chemistry C*, vol. 113, no. 8, pp. 3246–3253, 2009.
  - [17] S. C. Pillai, P. Periyat, R. George et al., “Synthesis of high-temperature stable anatase TiO<sub>2</sub> photocatalyst,” *The Journal of Physical Chemistry C*, vol. 111, no. 4, pp. 1605–1611, 2007.
  - [18] C. Sanchez, J. Livage, M. Henry, and F. Babonneau, “Chemical modification of alkoxide precursors,” *Journal of Non-Crystalline Solids*, vol. 100, no. 1–3, pp. 65–76, 1988.
  - [19] H. Khan and D. Berk, “Sol–gel synthesized vanadium doped TiO<sub>2</sub> photocatalyst: physicochemical properties and visible light photocatalytic studies,” *Journal of Sol-Gel Science and Technology*, vol. 68, no. 2, pp. 1–13, 2013.
  - [20] H. Zhang and J. F. Banfield, “Understanding polymorphic phase transformation behavior during growth of nanocrystalline aggregates: insights from TiO<sub>2</sub>,” *The Journal of Physical Chemistry B*, vol. 104, no. 15, pp. 3481–3487, 2000.
  - [21] H. Khan and I. K. Swati, “Fe<sup>3+</sup>-doped Anatase TiO<sub>2</sub> with d–d transition, oxygen vacancies and Ti<sup>3+</sup> centers: synthesis, characterization, UV–vis photocatalytic and mechanistic studies,” *Industrial and Engineering Chemistry Research*, vol. 55, no. 23, pp. 6619–6633, 2016.
  - [22] N. T. Nolan, D. W. Synnott, M. K. Seery, S. J. Hinder, A. V. Wassenhoven, and S. C. Pillai, “Effect of N-doping on the photocatalytic activity of sol–gel TiO<sub>2</sub>,” *Journal of Hazardous Materials*, vol. 211–212, pp. 88–94, 2012.
  - [23] H. Khan and D. Berk, “Synthesis, physicochemical properties and visible light photocatalytic studies of molybdenum, iron and vanadium doped titanium dioxide,” *Reaction, Kinetics, Mechanism and Catalysis*, vol. 111, no. 1, pp. 1–22, 2013.
  - [24] N. T. Nolan, M. K. Seery, and S. C. Pillai, “Spectroscopic investigation of the anatase-to-rutile transformation of sol–gel-synthesized TiO<sub>2</sub> photocatalysts,” *The Journal of Physical Chemistry C*, vol. 13, no. 36, pp. 16151–16157, 2009.
  - [25] V. Zelenak, Z. Vargova, and K. Gyoryova, “Correlation of infrared spectra of zinc(II) carboxylates with their structures,” *Spectrochimica Acta Part A: Molecular and Biomolecular Spectroscopy*, vol. 66, no. 2, pp. 262–272, 2007.
  - [26] Y. Lu and J. D. Miller, “Carboxyl stretching vibrations of spontaneously adsorbed and LB-transferred calcium carboxylates as determined by FTIR internal reflection spectroscopy,” *Journal of Colloid and Interface Science*, vol. 256, no. 1, pp. 41–52, 2002.
  - [27] M. T. Tsai, “Hydrolysis and condensation of forsterite precursor alkoxides: modification of the molecular gel structure by acetic acid,” *Journal of Non-Crystalline Solids*, vol. 298, no. 2–3, pp. 116–130, 2002.
  - [28] R. Beranek and H. Kisch, “Tuning the optical and photoelectrochemical properties of surface-modified TiO<sub>2</sub>,” *Photochemical and Photobiological Sciences*, vol. 7, no. 1, pp. 40–48, 2008.
  - [29] M. R. Bayati, A. Z. Moshfegh, and F. F. Golestani, “On the photocatalytic activity of the sulfur doped titania nano-porous films derived via micro-arc oxidation,” *Applied Catalysis A: General*, vol. 389, no. 1–2, pp. 60–67, 2010.
  - [30] G. Yang, Z. Jiang, H. Shi, T. Xiao, and Z. Yan, “Preparation of highly visible-light active N-doped TiO<sub>2</sub> photocatalyst,” *Journal of Materials Chemistry*, vol. 20, no. 25, pp. 5301–5309, 2010.
  - [31] T. He, X. Guo, K. Zhang, Y. Feng, and X. Wang, “Synthesis and characterization of B-N co-doped mesoporous TiO<sub>2</sub> with enhanced photocatalytic activity,” *RSC Advances*, vol. 4, no. 12, pp. 5880–5886, 2014.
  - [32] B. Li, X. Cheng, X. Yu, L. Yan, and Z. Xing, “Synthesis and characterization of Fe-N-S-tri-doped photocatalyst and its enhanced visible light photocatalytic activity,” *Advances in Materials Science and Engineering*, vol. 2012, Article ID 348927, 5 pages, 2012.

- [33] C. D. Valentin, E. Finazzi, G. Pacchioni et al., "N-doped TiO<sub>2</sub>: theory and experiment," *Chemical Physics*, vol. 339, no. 1–3, pp. 44–56, 2007.
- [34] D. Li, H. Haneda, S. Hishita, N. Ohashi, and N. K. Labhsetwar, "Fluorine-doped TiO<sub>2</sub> powders prepared by spray pyrolysis and their improved photocatalytic activity for decomposition of gas-phase acetaldehyde," *Journal of Fluorine Chemistry*, vol. 126, no. 1, pp. 69–77, 2005.
- [35] D. C. Cronmeyer, "Infrared absorption of reduced rutile TiO<sub>2</sub> single crystals," *Physical Review*, vol. 113, no. 5, pp. 1222–1226, 1959.
- [36] D. Ma, Y. Xin, M. Gao, and J. Wu, "Fabrication and photocatalytic properties of cationic and anionic S-doped TiO<sub>2</sub> nanofibers by electrospinning," *Applied Catalysis B: Environmental*, vol. 147, pp. 49–57, 2014.
- [37] M. A. Henderson, W. S. Epling, C. L. Perkins, C. H. F. Peden, and U. Diebold, "Interaction of molecular oxygen with the vacuum-annealed TiO<sub>2</sub>(110) surface: molecular and dissociative channels," *The Journal of Physical Chemistry B*, vol. 103, no. 25, pp. 5328–5337, 1999.
- [38] S. Zheng, Y. Cai, and K. E. O'Shea, "TiO<sub>2</sub> photocatalytic degradation of phenylarsonic acid," *Journal of Photochemistry and Photobiology A: Chemistry*, vol. 210, no. 1, pp. 61–68, 2010.
- [39] Z. Xu, C. Jing, F. Li, and X. Meng, "Mechanisms of photocatalytic degradation of monomethylarsonic and dimethylarsinic acids using nanocrystalline titanium dioxide," *Environmental Science and Technology*, vol. 42, no. 7, pp. 2349–2354, 2008.
- [40] D. B. Hernandez-Uresti, A. Vazquez, D. Sanchez-Martinez, and S. Obregon, "Performance of the polymeric g-C<sub>3</sub>N<sub>4</sub> photocatalyst through the degradation of pharmaceutical pollutants under UV-vis irradiation," *Journal of Photochemistry and Photobiology A: Chemistry*, vol. 324, pp. 47–52, 2016.
- [41] F. Peng, L. Cai, H. Yu, H. Wang, and J. Yang, "Synthesis and characterization of substitutional and interstitial nitrogen-doped titanium dioxides with visible light photocatalytic activity," *Journal of Solid State Chemistry*, vol. 181, no. 1, pp. 130–136, 2008.



**Hindawi**

Submit your manuscripts at  
<https://www.hindawi.com>

